Biophysical Journal
Article

Biophysical Society

Cholesterol Promotes Protein Binding by Affecting Membrane Electrostatics and Solvation Properties

Milka Doktorova,[1] Frederick A. Heberle,[2,3,4,*] Richard L. Kingston,[5] George Khelashvili,[6] Michel A. Cuendet,[6] Yi Wen,[7] John Katsaras,[2,4,8,9] Gerald W. Feigenson,[7] Volker M. Vogt,[7] and Robert A. Dick[7,*]

[1]Tri-Institutional PhD Program in Computational Biology and Medicine, Weill Cornell Medical College, New York, New York; [2]The Bredesen Center for Interdisciplinary Research and Graduate Education, University of Tennessee, Knoxville, Tennessee; [3]Joint Institute for Biological Sciences and [4]Biology and Soft Matter Division, Oak Ridge National Laboratory, Oak Ridge, Tennessee; [5]School of Biological Sciences, The University of Auckland, Auckland, New Zealand; [6]Department of Physiology and Biophysics, Weill Cornell Medical College, New York, New York; [7]Department of Biochemistry and Molecular Cell Biology, Cornell University, Ithaca, New York; [8]Department of Physics and Astronomy, University of Tennessee, Knoxville, Tennessee; and [9]Shull Wollan Center, Oak Ridge National Laboratory, Oak Ridge, Tennessee

ABSTRACT Binding of the retroviral structural protein Gag to the cellular plasma membrane is mediated by the protein's matrix (MA) domain. Prominent among MA-PM interactions is electrostatic attraction between the positively charged MA domain and the negatively charged plasma membrane inner leaflet. Previously, we reported that membrane association of HIV-1 Gag, as well as purified Rous sarcoma virus (RSV) MA and Gag, depends strongly on the presence of acidic lipids and is enhanced by cholesterol (Chol). The mechanism underlying this enhancement was unclear. Here, using a broad set of in vitro and in silico techniques we addressed molecular mechanisms of association between RSV MA and model membranes, and investigated how Chol enhances this association. In neutron scattering experiments with liposomes in the presence or absence of Chol, MA preferentially interacted with preexisting POPS-rich clusters formed by nonideal lipid mixing, binding peripherally to the lipid headgroups with minimal perturbation to the bilayer structure. Molecular dynamics simulations showed a stronger MA-bilayer interaction in the presence of Chol, and a large Chol-driven increase in lipid packing and membrane surface charge density. Although in vitro MA-liposome association is influenced by disparate variables, including ionic strength and concentrations of Chol and charged lipids, continuum electrostatic theory revealed an underlying dependence on membrane surface potential. Together, these results conclusively show that Chol affects RSV MA-membrane association by making the electrostatic potential at the membrane surface more negative, while decreasing the penalty for lipid headgroup desolvation. The presented approach can be applied to other viral and nonviral proteins.

INTRODUCTION

For HIV and Rous sarcoma virus (RSV), formation of an infectious form of the virus requires interaction of the viral structural protein Gag with the acidic inner leaflet of the plasma membrane (PM). The resulting lateral Gag-Gag interactions lead to the formation of a Gag lattice and subsequently a budding virus particle. The N-terminal matrix (MA) domain of Gag mediates interaction with the PM by responding to multiple signals, including electrostatic and hydrophobic interactions, and in some cases, specific interaction with lipid headgroups (1). Cholesterol (Chol), an abundant PM lipid, is a critical component of the viral envelope (2). Compared with the PM, the viral envelope is enriched in sphingomyelin and anionic lipids, including phosphatidylserine (PS) and phosphatidyl(4,5)-inositol bisphosphate (PI(4,5)P2) (3–5). Moreover, viral budding sites colocalize with tetraspanin-rich domains (6). These data suggest that Gag selects or modulates compositionally distinct domains in the PM.

Neutron reflectometry (NR) has shown that for HIV and RSV Gag, the highly basic region of MA is oriented toward the membrane surface (7,8), and that the Gag conformation changes upon addition of a nucleic acid (9). One drawback of NR is the requirement of a supported lipid bilayer that can influence lipid diffusion (10) and mixing behavior (11). Moreover, NR is primarily sensitive to the time-averaged matter distribution in the direction perpendicular to the bilayer plane, whereas in-plane structural information is much more difficult to access. However, a related technique, small-angle neutron scattering (SANS), can provide

Submitted April 6, 2017, and accepted for publication August 9, 2017.

*Correspondence: heberlefa@ornl.gov or rad82@cornell.edu

Milka Doktorova, Frederick A. Heberle, and Robert A. Dick contributed equally to this work.

Editor: David Cafiso.

https://doi.org/10.1016/j.bpj.2017.08.055

information about both in-plane and out-of-plane bilayer structure. Because neutrons are scattered differently by protium (^{1}H) and hydrogen's stable isotope deuterium (^{2}H), mixtures of protiated and deuterated lipids generate a strong in-plane contrast upon clustering or phase separation, resulting in a distinct SANS signature (12), thus providing a unique tool to probe lipid lateral organization (13). SANS can also easily be applied to liposomes of the type used in biochemical or nuclear magnetic resonance (NMR) analyses of protein-membrane interaction (14,15).

Complementing the time-averaged structural data from SANS, molecular dynamics (MD) simulations provide atomistic detail, allowing a focused examination of different protein binding modes and their dependence on membrane structure. For example, a coarse-grained MD study found that HIV MA can sequester multivalent but not monovalent acidic lipids upon anchoring in membranes without Chol (16). However, the cellular PM contains ~40 mol % Chol (17), and liposome binding of both RSV and HIV Gag is stimulated by physiological Chol concentrations in model membranes (18). Both in vitro and in silico experiments have shown that the addition of Chol to fluid bilayers causes significant structural changes, including increased bilayer thickness (19,20), increased headgroup spacing (21) and hydration (22), and reduced water penetration into the membrane hydrocarbon region (22,23).

Here, using SANS, MD simulations, and liposome binding assays, we investigated the mechanism by which Chol influences RSV MA membrane binding, and whether protein binding changes the structure or lateral organization of lipids in the bilayer. Our results show that in bilayers with a fixed concentration of acidic lipids, Chol promotes binding of RSV MA by making the electrostatic potential above the membrane surface more negative, while at the same time decreasing the energetic penalty for lipid headgroup desolvation. We also find that MA selectively binds to preexisting patches of acidic lipids, but does not significantly affect their structure or composition. These findings reveal the intrinsic ability of lipid membranes to modulate the electrostatically driven binding of charged molecules, and have important implications for interpreting in vitro binding data.

MATERIALS AND METHODS

Materials

Phospholipids were purchased from Avanti Polar Lipids (Alabaster, AL) as dry powders and dissolved in HPLC-grade chloroform. Lipid stock concentrations were determined by inorganic phosphate assay (24) with an error <2%. Cholesterol powder was purchased from Nu-Chek Prep (Waterville, MN) and prepared as chloroform stock solutions at defined concentration using standard gravimetric procedures. Ultrapure H_2O was obtained from a High-Q purification system (Wilmette, IL). D_2O (99.96%), deuterated Tris buffer (Tris-D11, 98%), and deuterated glycerol (glycerol-D8, 99%) were purchased from Cambridge Isotopes (Andover, MA). Deuterium chloride (DCl) and Tris(2-carboxyethyl)phosphine (TCEP) were purchased from Sigma-Aldrich (St. Louis, MO) and AMRESCO (Solon, OH), respectively. Buffer solutions were filtered through a prerinsed 0.2 μm filter before use.

Protein purification and liposome binding

Protein was purified as previously described (8) and stored at –80°C until use. Preparation of 100 nm extruded liposomes and binding reactions were performed as previously described (25). Briefly, all binding reactions were performed with 15 μg (4.7 μM) protein and 50 μg (328−431 μM) lipid in 200 μL at 20 mM Tris-HCl pH 8, and adjusted with buffer to the stated NaCl concentration. Binding reactions were subjected to centrifugation at 90,000 RPM (relative centrifugal force = 351,955 × g) in a TLA-100 rotor (Beckman Coulter, Brea, CA) for 45 min at 4°C to pellet the liposome-bound protein. Pelleted protein was subjected to sodium dodecyl-sulfate polyacrylamide gel electrophoresis analysis. Gels were stained with Coomassie Blue and then destained, and band intensity was determined by densitometry analysis using ImageQuant 5.2 (Molecular Dynamics, Sunnyvale, CA). Each binding reaction was repeated no fewer than four times. The binding data reported in Fig. 5 is the average, and error bars the SD, of measurements from these independent replicate samples.

SANS sample preparation

Lipid mixtures were prepared by transferring lipid and cholesterol chloroform stocks to a glass vial with a glass syringe. Organic solvent was removed with a nitrogen stream and gentle heating, followed by vacuum drying for >12 h. Dry lipid films were hydrated to 40 mg/mL total lipid concentration with liposome storage buffer (D_2O, 50 mM NaCl, 20 mM Tris-D11-DCl, 2 mM TCEP, pD 8), then vortexed vigorously to generate multilamellar vesicles. The multilamellar vesicle suspension was incubated for 1 h with intermittent vortexing, followed by 5 freeze/thaw cycles. Large unilamellar vesicles (LUVs) were prepared using a miniextruder (Avanti Polar Lipids) by passing the lipid suspension 31 times through a single 100-nm-pore-size polycarbonate filter. RSV-MA solution in protein storage buffer (D_2O, 375 mM NaCl, 20 mM Tris-D11-DCl, 2 mM TCEP, 5 wt % glycerol-D8, pD 8) at 40 mg/mL was prepared from protein in H_2O buffer by serial dilution and centrifugal filter concentration.

Samples for SANS measurements were prepared by combining and pipette-mixing 57 μL of the protein solution with 150 μL of the liposome solution and 390 μL pure D_2O. By design, a small excess of osmolytes in the vesicle interior (liposome storage buffer) compared to the extravesicular buffer after mixing (D_2O, 48 mM NaCl, 7 mM Tris-D11-DCl, 0.7 mM TCEP, 0.5 wt % glycerol-D8, pD 8) generated slightly hypotonic conditions that tended to swell the vesicles. This precaution was necessary to avoid distorted or partially collapsed vesicles, which result in complex scattering curves that cannot be analyzed with conventional spherical shell form factors. The final protein and lipid concentrations of SANS samples were 3.8 mg/mL (0.227 mM) and 10 mg/mL (13–16 mM, depending on the lipid composition), respectively, with all protein located in the extravesicular fluid. At these concentrations, enough protein was present to cover 70–80% of the vesicle surface area, assuming complete binding and average lipid and protein cross-sectional areas of 48–65 and 1375 Å^2, respectively. The actual surface coverage determined by analysis of the scattering curves was 35–40% (Table S2), indicating that approximately half of the protein was bound to vesicles, with half remaining free in solution.

SANS data collection

SANS measurements were performed using the BL-6 extended Q-range small-angle neutron scattering (EQ-SANS) instrument of the Spallation Neutron Source at Oak Ridge National Laboratory, Oak Ridge, TN. Samples were loaded into 2 mm path-length quartz banjo cells (Hellma

USA, Plainview, NY) and mounted in a temperature-controlled cell holder with ~1°C accuracy. EQ-SANS data were taken at a 2.5 m sample-to-detector distance with a 2.5–6.0 Å wavelength band for a total scattering vector of $0.01 < q < 0.5$ Å^{-1}. Scattered neutrons were collected with a 2D (1 × 1 m) ^{3}He position-sensitive detector (ORDELA, Oak Ridge, TN) with 256 × 192 pixels. The 2D data were reduced using the software package Mantid (26). During reduction, data were corrected for detector pixel sensitivity, dark current, and sample transmission, as well as background scattering from buffer. The 1D intensity $I(q)$ ($q = 4\pi \sin(\theta)/\lambda$, where λ is the neutron wavelength and 2θ is the scattering angle relative to the incident beam), was obtained by radial averaging of the corrected 2D data.

SANS data analysis

SANS curves were fit with a laterally heterogeneous core-shell form factor (27) to account for coherent scattering contributions from both transverse (out-of-plane) and lateral (in-plane) neutron scattering length density (NSLD) variation within the vesicle (a detailed description of the model is provided in the Supporting Material). As shown schematically in Fig. S2 *A*, transverse NSLD variation arises primarily from the different atomic composition of the lipid headgroup and hydrocarbon layers, whereas lateral NSLD variation is primarily due to lipid clustering resulting from nonideal mixing or phase separation, and is pronounced when some lipid species are selectively deuterated. Both the transverse and lateral NSLD variation are further influenced by the presence of surface-bound protein, which has a different NSLD than lipid or water.

The heterogeneous core-shell form factor requires as input the transverse NSLD profiles of the domain and continuous phases, as well as the size, surface coverage, and spatial arrangement of the domains (Fig. S2 *A*). Our analysis allowed for the possibility of nonrandom lipid mixing, which we modeled as a PS-rich domain phase surrounded by a continuous phase depleted in PS. The compositions of the two phases were allowed to vary in the fit, but not independently; given a fixed overall vesicle composition, a domain composition, and phase area fractions, the composition of the continuous phase was constrained by material balance. Following Kučerka et al. (28), NSLD profiles for the domain and continuous phases were derived from underlying lipid volume probability distributions, modeled as the sum of separate distributions for the lipid headgroups and hydrocarbon chains. The total unit cell volume was calculated as a mole-fraction weighted sum of lipid component volumes obtained from the literature (Table S3) and constrained in the fit, leaving adjustable parameters for the area per lipid A_L and headgroup thickness D_H. Additional structural parameters, including the total bilayer thickness D_B and the hydrocarbon thickness $2D_C$, were derived from relationships between the adjustable parameters and the lipid headgroup and hydrocarbon volumes as described in the Supporting Material. For MA-containing samples, a Gaussian volume probability distribution with adjustable parameters for position (z_p) and width (σ_p) was added to the domain phase. NSLD profiles were then obtained as a sum of the separate headgroup, hydrocarbon, and protein volume probability distributions multiplied by their respective total scattering lengths. Lateral structure was modeled by assuming round domains with a 21 Å radius (corresponding to a cross-sectional area of 1375 Å^2 for an MA monomer) that were randomly arranged on the vesicle surface. The in-plane contributions to the vesicle form factor were calculated to 200 expansion orders and included an adjustable parameter for the fraction of the vesicle surface area occupied by domains, a_p.

For each nominal sample composition (i.e., POPC/POPS 70:30 mol % and POPC/POPS/Chol 34:30:36 mol %), separate SANS samples with different contrast were prepared using the four permutations of protiated and palmitoyl chain-perdeuterated variants of the two phospholipids (i.e., POPC or POPC-D31, mixed with POPS or POPS-D31; Fig. S2, *C*–*F*). Fitting was implemented in the softwares Mathematica 11.0 (Wolfram Research, Champaign, IL) and MATLAB R2013b (The MathWorks, Natick, MA). Each data set was fit independently, and the reported structural parameters represent the mean and SD from the four fits. A complete list of the structural parameters is found in Table S2.

High-resolution structure of MA

To provide the structural models required for the detailed interrogation of molecular interactions, we crystallized full-length RSV MA (155 amino acids) and determined an experimentally phased x-ray structure at 2.8 Å resolution. Residues 1−102 were well resolved but there was no interpretable electron density for the remainder of the molecule. We therefore characterized a truncated variant (MA2−102) with the disordered region removed. This variant crystallized in the same form as the full-length molecule (space group $I4_122$), and also in an alternate form (space group $I4_1$). Structures were determined to 3.2 and 1.8 Å resolution, respectively. The three crystallographic models (Table S1) differ in detail from an earlier NMR solution structure for the first 88 amino acids (29). This likely reflects both the limited restraint set and the methodology used to derive the NMR model (30). However, consistent with NMR relaxation measurements (29), the basic surface loop (residues 14−22), which is critical for membrane association, is the most mobile element in the crystallographic models. For crystals in the space group $I4_122$, the final helix of the N-terminal domain (helix 6, residues 89−102) interdigitates with the corresponding helix from a neighboring molecule, forming a symmetric dimer (Fig. S1 *A*). In contrast, for space group $I4_1$ crystals, the C-terminal sequence is disordered and neither helix 6 nor the dimer is observed. Because deletions in the C-terminal region of MA (amino acids 87−155) do not abrogate viral budding and infectivity (31), and because there is no evidence that MA dimerizes in solution (8) or when membrane associated (32), it is likely that the crystallographic dimer is biologically irrelevant. Because the monomer structure was not available when our MD simulations were carried out, one subunit of the dimer was adapted as the working model for the in silico experiments reported here (see below and Fig. S1).

MD simulations

All MD simulations were performed with the software NAMD (33) and the CHARMM36 force field for lipids and protein (34,35). The simulations were run with a 2-fs time-step with all bonds to hydrogens constrained, in NPT ensemble with semiisotropic (for bilayer simulations) or isotropic (for water box simulation) pressure coupling at 1 bar and 293 K. Temperature and pressure were controlled with a Langevin thermostat and barostat, with a damping parameter set to 5 ps^{-1}, a piston period of 200 fs, and a piston decay of 50 fs. The vdwForceSwitching option in NAMD was used for all membrane simulations (36). The van der Waals cutoff and switching distances were set to 12 and 10 Å, respectively. Particle mesh Ewald was used with a grid spacing of 1.0 Å.

To determine a starting conformation for MA in subsequent MA-membrane simulations, we first simulated one monomer from the crystal dimer structure of MA (Fig. S1 *A*) in an aqueous environment consisting of a water box with 13,470 water molecules and 20 mM NaCl. Following the hypothesis that the large angle between the C-terminal helix of MA (residues 91–102) and the rest of the protein body was dimer-specific and would not be a stable conformation of the MA monomer, we fixed the C-terminal helix in space and monitored the relaxation dynamics of the rest of the protein. The system was energy minimized for 5400 steps, then run for 500 ps with a 1-fs time step, followed by a production run of 110 ns. In the course of the simulation, the protein body moved closer to the C-terminal helix, adopting a stable compact conformation (Fig. S1, *B* and *C*). The protein coordinates from the last frame were used as the starting MA conformation for the MA-membrane simulations described below.

The two simulated bilayers (POPC/POPS 70:30 mol % and POPC/POPS/Chol 34:30:36 mol %) were taken from (37). After the production runs (191 and 270 ns, respectively), MA was placed on one or both sides of the bilayer and oriented with respect to the membrane surface in a way that optimized

interactions between lysines and the surface as described for HIV MA (7), and for RSV MA (38). Multiple replica simulations of the bilayer-protein systems in 50 mM NaCl were run for ~200 ns each and analyzed jointly as described in the Supporting Material.

RESULTS AND DISCUSSION

MA binds to lipid headgroups without perturbing the overall bilayer structure

We used SANS to determine the bilayer structure before and after RSV MA binding to 100-nm-diameter unilamellar vesicles (i.e., LUVs, also referred to as "liposomes" throughout) at 20°C and 50 mM NaCl. Motivated by previous work showing that cholesterol enhances MA binding (18), we examined two compositions having a fixed amount of the negatively charged lipid POPS, namely POPC/POPS 70:30 mol % and POPC/POPS/Chol 34:30:36 mol %. The POPS concentration was based on estimates of the concentration of charged lipids in the PM inner leaflet (32 mol %; Table S4). These compositions allow for a direct comparison that isolates the effect of cholesterol, and are simple enough to be tractable in a SANS analysis. Scattering data (Fig. S2, *C–F*) were analyzed with a model describing the projected distribution of matter (i.e., lipid headgroups, lipid chains, protein, and water) along the bilayer normal, as a function of distance from the bilayer center. In particular, we used volume probability distributions to model the relative locations of the different components, which enabled the determination of bilayer structural parameters including area per lipid, total bilayer thickness, hydrocarbon thickness, and the position of the bound protein within the bilayer and the transverse water distribution (Supporting Material).

Fig. 1 shows the lipid and protein matter distribution for bilayers without (Fig. 1 *B*) and with Chol (Fig. 1 *C*) obtained from SANS analysis. The bulk of the protein density (*purple curves*) resides above the lipid headgroups (*green curves*), although a small degree of overlap suggests that some residues are able to intercalate between lipid headgroups. Importantly, practically no protein density overlaps with the lipid hydrocarbon region (*red curves*), an indication that MA does not penetrate the bilayer's hydrophobic core, and binds in a manner consistent with electrostatic attraction to the negatively charged headgroup region. Structural parameters recovered from our analysis are in agreement with published values for POPC and POPS bilayers (39,40). The replacement of 36 mol % of POPC with Chol (mimicking physiological Chol concentrations and charged-to-neutral headgroup ratios) reduced the area per lipid (defined here and throughout to include Chol) by ~25%, from 63.0 to 48.8 $Å^2$ (Fig. 1 *D*). Hydrocarbon chain thickness increased by nearly 5 Å, from 29.1 to 33.8 Å (Fig. 1 *E*), also consistent with published data (41). Neither the area per lipid nor the hydrocarbon thickness changed significantly in the presence of MA, suggesting that protein binding does not perturb the bilayer structure. This finding was supported by electron spin resonance (ESR) measurements showing that the lipid acyl chain order parameter did not change in the presence of MA (Fig. S3). A complete list of structural parameters obtained from the SANS analysis is found in Table S2.

MA binds to POPS clusters

Neither POPC/POPS nor POPC/POPS/Chol bilayers are phase separated at 20°C (L. Goh, personal communication). Such mixtures may nevertheless be heterogeneous on small (<5 nm) length scales (42). To a first approximation, nonideality arises from the different nearest-neighbor interactions of unlike lipids (e.g., POPC and POPS). Interactions between unlike phospholipids can be unfavorable (43), resulting in clustering of like lipids to reduce unlike contacts. To account for the possibility of such nonrandom lipid mixing, we analyzed our scattering data using a form factor appropriate for laterally heterogeneous vesicles (27). We analyzed four combinations of protiated and palmitoyl chain-perdeuterated variants of POPC and POPS (Fig. S2 *B*) to take full advantage of neutron contrast for detecting possible lateral segregation of these lipids. The scattering model allowed for two distinct bilayer environments whose compositions were varied in the fit while maintaining overall matter balance (Fig. S2 *A*). In the analysis of data from MA-containing samples, the compositions of the protein-bound and protein-free portions of the bilayer were also allowed to vary. Consistent with previous reports (44), the SANS analysis indicated a patchy bilayer characterized by lipid clusters that are enriched approximately twofold in POPS (Fig. 1 *F*). In MA-containing samples, we found a similar amount of PS enrichment in the protein-bound bilayer composition (Fig. 1 *F*). The addition of Chol did not have a significant effect on the extent of nonideal mixing of POPC and POPS, either in the presence or absence of MA.

Although the lateral heterogeneity observed in our SANS analysis is statistically significant, the large uncertainties in PS enrichment (Fig. 1 *F*) do not allow us to draw any conclusions regarding the ability of MA to sequester charged lipids upon binding. To test this possibility, we applied a previously developed computational method based on continuum mean-field theory (45,46) to quantify the extent of lipid redistribution in response to protein binding to an ideally mixed bilayer, and to calculate changes in the corresponding adsorption free energy upon the demixing process (Fig. S4; Supporting Material). Our calculations predict that MA cannot effectively sequester POPS as has been shown previously for other proteins (see (46) and references therein); minimal lipid segregation was achieved, which produced an insignificant change in the adsorption free energy (<1 k_BT). Taken together with the SANS results, this calculation suggests that MA does not induce lipid redistribution. Rather, the protein takes advantage of the inherent

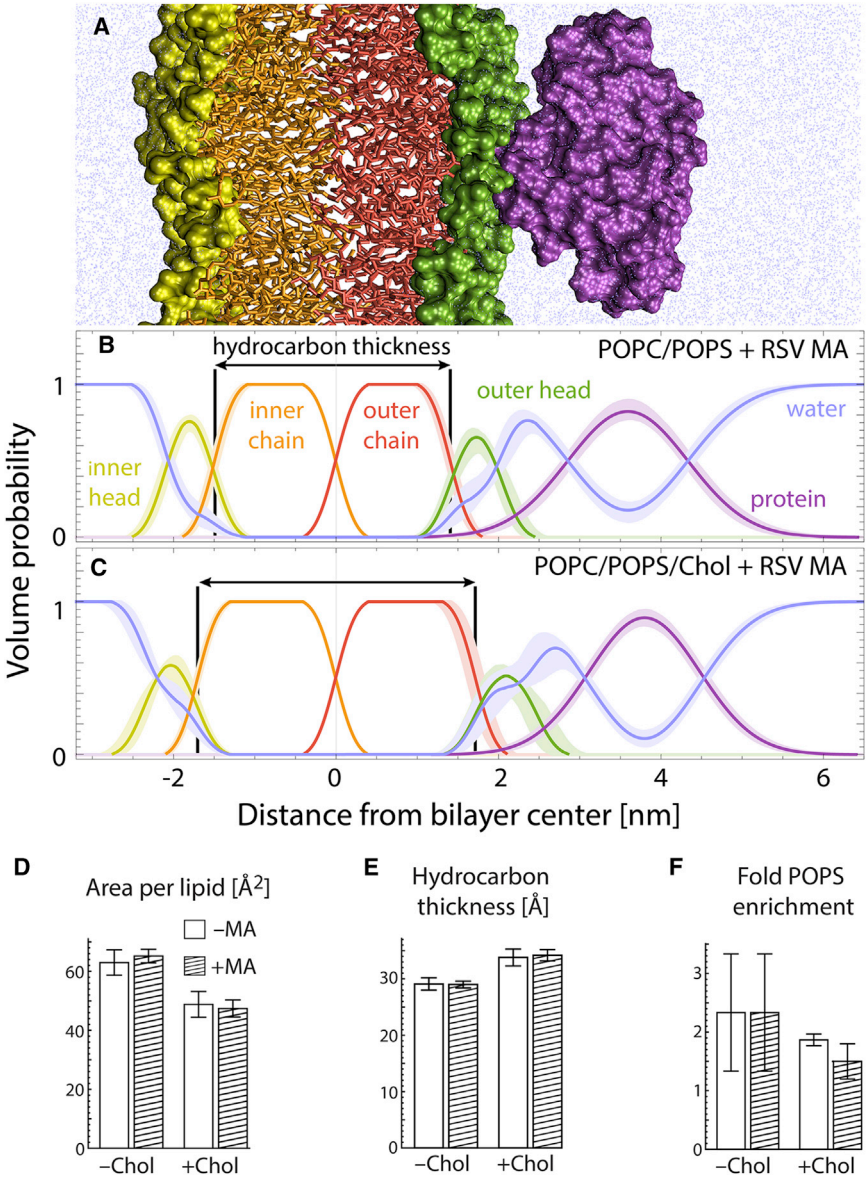

FIGURE 1 MA binds peripherally to lipid bilayers with minimal structural perturbation. (*A*) An MD simulation snapshot showing the different lipid and protein components modeled in the SANS analysis: inner leaflet headgroups (*yellow*) and chains (*orange*), outer leaflet chains (*red*) and headgroups (*green*), protein (*purple*), and water (*blue*). Below the cross-sectional view, the volume probability profiles obtained from experimental SANS data are displayed (*thick lines* surrounding the volume probability profiles reflect uncertainties): POPC/POPS 70:30 mol % with bound RSV MA (*B*); POPC/POPS/Chol 34:30:36 mol % with bound RSV MA (*C*). (*D*–*F*) Structural parameters obtained from SANS analysis of POPC/POPS bilayers without and with Chol, in the absence (*white bars*) or presence (*hatched bars*) of RSV MA: average area per molecule (*D*); lipid hydrocarbon thickness (*E*); and fold-enrichment of POPS over the average composition in PS-rich clusters (*F*). The reported structural parameters and errors represent the mean and SD from independent fits to four different neutron contrast data sets as described in the text and Supporting Material. A complete list of structural parameters is found in Table S2.

patchiness of the nonideally mixed bilayers, binding to the membrane primarily at sites already enriched with anionic lipids.

Cholesterol enhances MA lysine-membrane contacts

To investigate the atomic-level details of MA-membrane interactions, we performed MD simulations mimicking the SANS experimental conditions, i.e., monomeric MA in the presence of a lipid membrane composed of either POPC/POPS at 70:30 mol % (Fig. 2 *A*), or POPC/POPS/Chol at 34:30:36 mol % (Fig. 2 *B*) in 50 mM NaCl solution at 20°C. The MA structure used as a starting point in these simulations was obtained from the monomer of the dimer crystal after relaxation in water (see Materials and Methods), and is similar to the independently determined monomer crystal structure (the backbone RMSD between the two structures is 2.8 Å; Fig. S1 *D*).

The protein's secondary structure remained stable during the simulations (Fig. S6 *A*), and the protein density did not penetrate further than the lipid headgroup region in either system (Fig. S5), consistent with the SANS results (Fig. 1, *B* and *C*). However, in the presence of Chol the helices' tilts changed slightly, facilitating the exposure of K13, K18, K24, and K72 to the membrane (Fig. S6 *C*). Of the protein's 10 lysine residues, two did not interact with either the POPC/POPS or POPC/POPS/Chol bilayer, whereas six exhibited a greater number of contacts with the +Chol membrane (Fig. 2 *C*). The slight conformational changes of the protein were accompanied by a moderate increase in the number of instantaneous lysine-POPS contacts

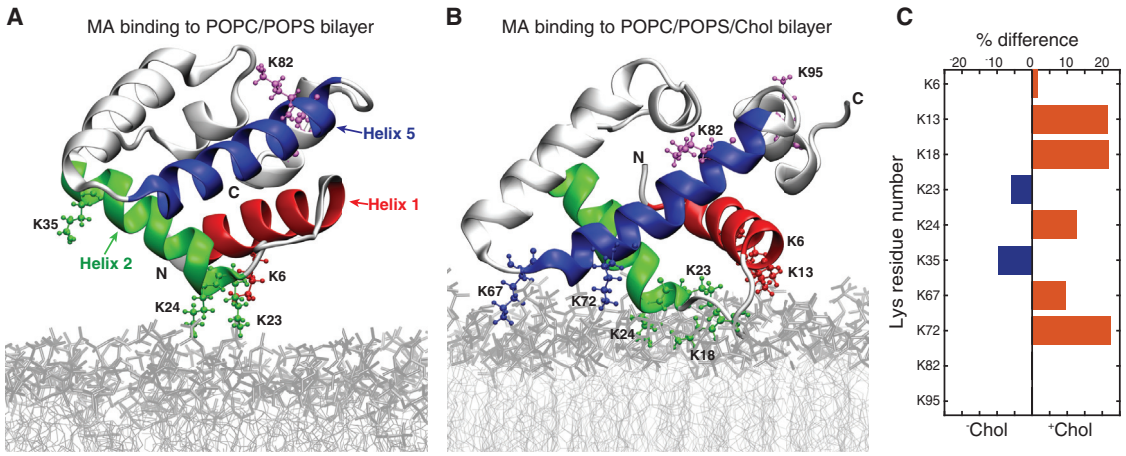

FIGURE 2 Cholesterol enhances MA-membrane contacts. Given here are snapshots of MA interacting with POPC/POPS (*A*) and POPC/POPS/Chol (*B*) bilayers after 100 ns of simulation (for corresponding movies, see Movie S1, *A* and *B*). The protein is displayed in silver with specific lysine residues labeled and shown in space-fill representation ("N" and "C" denote the protein termini). Lipid tails and headgroups are shown as light and dark gray lines, respectively, and water and ions are omitted for clarity. (*C*) Shown is the difference in the percent time that MA lysine residues spend in contact with the bilayer in the absence and presence of Chol, where contact is defined as a distance not greater than 3 Å between any residue atom and any lipid atom. K13, K18, and K72 spend a mean 22% more time in contact with the membrane when Chol is present, whereas K82 and K95 are never in contact with either bilayer.

(Fig. S6 *B*). For example, during the last 100 ns of the simulations when the bilayer contained Chol, up to seven lysine residues (as opposed to six in the POPC/POPS bilayer) simultaneously came into contact with PS, and the probability of a single PS lipid interacting with three lysine residues was 25 times greater than in the POPC/POPS bilayer. These results are consistent with a stronger electrostatic interaction between MA and the Chol-containing membrane.

The modes of RSV MA-membrane interaction observed in the simulations have been implicated in functional phenotypes in vivo (47). In the simulations, the basic residues in the first 35 amino acids of the protein were actively engaged in contacts with the bilayer. The exception was K35, which spent <20% of the time close to the membrane, consistent with the unaffected budding of virus particles in the K35Q mutant (47). In the simulations, neither K82, R61, or R85 (K82, K61, and K85 in the RSV strain studied in (47)) came in contact with the lipids, which agrees with the less severe reductions in virus particle release observed in the double mutants of K61Q/K82Q and K61Q/K85Q. Furthermore, in contrast to E25 and E70, the location of D52 on helix 4 keeps that residue away from the bilayer surface in the simulations, helping clarify the experimental observation of full versus partial rescue of a budding-defective mutant upon lysine substitution of the glutamic or aspartic acids, respectively (47).

Cholesterol increases the membrane surface charge density

Neither SANS nor MD simulations provided evidence for a direct interaction between MA and Chol, although SANS showed a reduction in area per lipid and an increase in hydrocarbon thickness for Chol-containing bilayers (Fig. 1, *D* and *E*). We therefore hypothesized that Chol indirectly influences MA binding by inducing changes in the bilayer structure that promote electrostatic interactions with the protein. To test this hypothesis, we first compared the structural properties of the two simulated bilayers in the absence of protein. It is important to note that because the ratio of negative charge to total lipid was fixed, the PC/PS ratio in the –Chol and +Chol bilayers was different (7:3 and 3.4:3, respectively). This choice was made to isolate the effects of cholesterol without changing the total negative charge.

Incorporation of Chol increased the lipid acyl chain order parameter by >65% (Fig. S6 *D*), consistent with ESR measurements (18). This change was accompanied by a 28% decrease in the average area per lipid from 60.9 to 43.5 $Å^2$, and a 6 Å increase in bilayer thickness from 40.5 to 46.9 Å, similar to SANS results (Fig. 1, *D* and *E*; Table S2). The reduction of bilayer area led to an increase in the PS surface density: for example, a 6.5 × 6.5-nm membrane patch would contain on average 42 or 60 charged headgroups in the absence or presence of 36 mol % Chol, respectively. The greater PS area density increased the bilayer's negative surface charge density (i.e., charge per unit area), which together with the lower PC/PS headgroup ratio (see Fig. S7 for the individual contributions of PC and PS to the charge density) completely eliminated the small peak of positive charge density observed in the –Chol bilayer, thus making electrostatic interactions with the +Chol membrane more favorable (Figs. 3 and S7).

To relate the changes in surface charge density to MA binding, we calculated the bilayer electrostatic potential (defined here and henceforth as 3 Å above the surface) using nonlinear

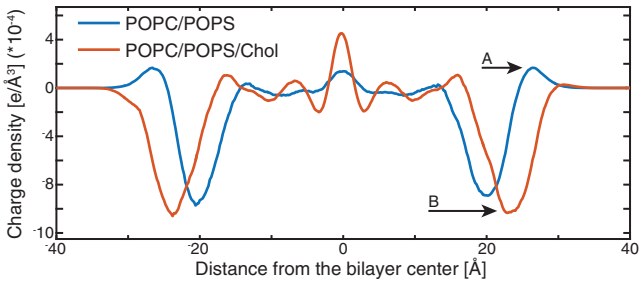

FIGURE 3 Cholesterol influences the membrane surface charge density. Charge distribution along the bilayer normal is calculated from the two simulated bilayers in the absence of MA. Addition of Chol increases the negative charge density in the headgroup region (*arrow B*), eliminating the peak of positive density at the water-lipid interface present in the POPC/POPS bilayer (*arrow A*). See Fig. S7 for the individual contributions of the membrane components.

Poisson-Boltzmann theory and the Gouy-Chapman model of the electrical double layer (48). The potential is a function of salt concentration, temperature, and surface charge density, with the latter calculated as the ratio of POPS mole fraction to the average area per lipid and having units of $e^-/Å^2$ (the reference potential in the bulk water far from the surface is zero). This formulation assumes that the charges are uniformly distributed on a continuum flat surface and therefore reports an average surface potential. Calculations based on conditions used in the MD simulations yielded potentials of –67 and –76 mV for the respective −Chol and +Chol bilayers, suggesting that the preference of MA for Chol-containing membranes is due to a stronger electrostatic attraction, because MA bears a net +3 charge.

Nonideal mixing of POPC and POPS lipids has a small effect on surface potential

Bilayers for MD simulations were constructed from an initially random lateral arrangement of phospholipids and Chol by using CHARMM-GUI (49). In light of the SANS finding of POPS clusters (Fig. 1 *F*), and because the simulation length of ~200 ns did not allow sufficient time for lipids to explore their conformational space through lateral diffusion, it is important to independently examine the effect of nonideal mixing on the bilayer's electrostatic potential. To this end, we performed Monte Carlo lattice simulations of a binary mixture of neutral and charged lipids in a 70:30 ratio, to obtain their equilibrium lateral distribution (Supporting Material). In this simple model, the lipid distribution is a function of a single adjustable parameter, the excess mixing energy ΔE_m of a PC/PS pair, which accounts for all nonideal interactions between these lipids (43). To examine different degrees of nonideal mixing we varied ΔE_m from zero (i.e., random mixing) to +0.5 kBT, which is just below the threshold for complete phase separation (50).

Static snapshots of the equilibrium lipid distributions with an increasing degree of nonideal mixing are shown in Fig. S8 (see Supporting Material for details). Also shown (Fig. S8, *lower panels*) are corresponding maps of the electrostatic surface potential relative to that of a uniform bilayer with 30 mol % charged lipids (Supporting Material). Although some patchiness of the potential is observed with increasing nonideality, in most cases the local potential varied by <10% from the average value, indicating that for low to moderate degrees of nonideal mixing the average potential calculated with the uniform Gouy-Chapman model is a reasonable approximation for the potential above the bilayer surface. Taken together with the SANS results showing similar degrees of nonideal mixing of POPC and POPS in the presence and absence of Chol, as well as the calculated 13% decrease in the average potential in the +Chol membrane, these findings suggest that nonideal mixing cannot account for the Chol-enhanced MA/bilayer interaction observed both in vitro (18) and in silico (this work).

Cholesterol increases the MA/bilayer electrostatic interaction and decreases the penalty for headgroup desolvation

To examine the specific energetic contributions of the protein and bilayer in the MA-membrane interaction, we used the molecular mechanics-generalized Born surface area (MM-GBSA) approach to estimate the binding free energy ΔG_{bind} of MA with the POPC/POPS and POPC/POPS/Chol bilayers, based on conformations sampled in the MD simulations (51,52). In the MM-GBSA framework, ΔG_{bind} is approximated as the sum of the interaction energy of the two binding partners (here, MA and bilayer) in vacuum $\Delta E_{\text{int}}^{\text{vac}}$, and the penalty for displacing water molecules upon protein binding. The latter is expressed as a difference in the energetic cost for desolvating the MA-bilayer complex and each partner separately, and is referred to as $\Delta\Delta G_{\text{solv}}$.

Our analysis showed that in the presence of Chol, the binding free energy was >4 kcal/mol more favorable than in the absence of Chol (–5.8 ± 0.3 vs. –1.6 ± 0.2 kcal/mol, respectively). Decomposition of ΔG_{bind} into electrostatic and desolvation contributions confirmed the much stronger electrostatic interaction of MA with the Chol-containing bilayer (–1531 vs. –1215 kcal/mol for +Chol and –Chol bilayers, respectively), while also revealing a similar trend in the polar desolvation penalties (1552 vs. 1242 kcal/mol), as shown in Table S5. When the two partners bind, the favorable electrostatic attraction between them is partially offset by the displacement of water molecules from the binding interface, which incurs an unfavorable desolvation penalty resulting from the high dielectric strength of water and charge screening by the salt.

Further insight was gained by decomposing $\Delta G_{\text{bind}} = \Delta E_{\text{int}}^{\text{vac}} + \Delta\Delta G_{\text{solv}}$ into the separate contributions from each binding partner (52,53). Whereas the balance between $\Delta E_{\text{int}}^{\text{vac}}$ and $\Delta\Delta G_{\text{solv}}$ for MA was similar in the two MA-bilayer systems (Fig. 4 *A*, *blue bars*), the energetic

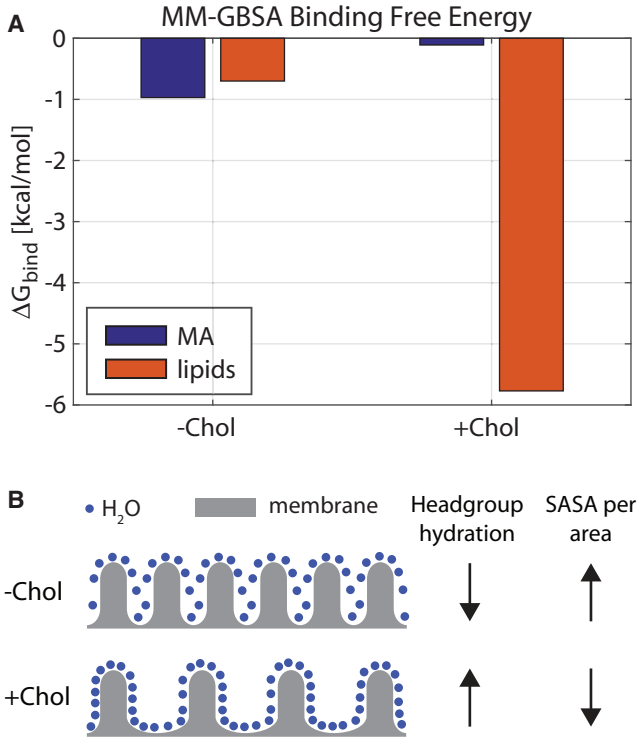

FIGURE 4 Cholesterol decreases the energetic penalty for lipid desolvation. (*A*) Given here are contributions of MA and lipids to the total binding free energy ΔG_{bind} of the MA-bilayer complex estimated using the MM-GBSA method. Each energetic contribution is the sum of the interaction energy in vacuum for the respective system and the solvation penalty calculated separately for MA and the lipids. The presence of Chol results in a 5 kcal/mol reduction in the solvation penalty of the lipids relative to ΔE_{int}^{vac}, resulting in a more favorable bilayer contribution to ΔG_{bind} compared to the PC/PS bilayer. For a detailed breakdown of the energy contributions and details of the underlying calculation, see Supporting Material. (*B*) A schematic illustration of the lipid headgroups (*gray*) on the bilayer surface in the +Chol and –Chol membranes, and the water molecules that solvate them (*blue dots*). Due to the area occupied by Chol itself, there are fewer lipid (PC or PS) headgroups in a bilayer patch of given size. Thus, even though Chol increases the number of bound waters per headgroup, it decreases the SASA per unit area of the bilayer (see text). Note that the spacing between the lipid headgroups in the +Chol schematic has been exaggerated to emphasize the lower packing density in this region.

cost for desolvating the lipids was lower for the +Chol bilayer, resulting in a more favorable MA-membrane interaction energy (Fig. 4 *A*, *orange bars*). The desolvation penalty is closely related to both the charge density and the solvent-accessible surface area (SASA) of the binding partners. Thus, the smaller desolvation penalty of the +Chol bilayer could be due to either a lower charge density, and/or smaller solvent-exposed molecular surface to desolvate in the presence of Chol. The area of the MA shadow (defined by the projection of the MA coordinates onto the bilayer plane) in the two bilayers was practically identical (Fig. S9 *B*), and the +Chol bilayer had on average one more POPS lipid than the –Chol bilayer (Fig. S9 *E*), thereby excluding the former possibility.

To test for the latter, we compared the SASA of the top leaflet patch in the MA shadow in the two bilayers. As expected, the +Chol bilayer had a significantly smaller SASA than the –Chol bilayer (Fig. S9 *A*). At first glance, a smaller SASA in the presence of Chol suggests fewer waters per lipid. Interestingly, a count of the number of waters within 3 Å of a POPC or POPS lipid revealed that, consistent with experimental data (22), lipids were in fact better hydrated in the +Chol bilayer, having roughly 13.3 waters/headgroup compared to 12.3 in the Chol-free bilayer (Fig. S9 *C*). However, due to the surface area occupied by Chol itself, there were on average four fewer lipid headgroups under the protein in the presence of Chol (Fig. S9 *D*). This resulted in ~30 fewer lipid-bound waters in the MA shadow in the +Chol bilayer compared to the –Chol bilayer (226 vs. 258), in agreement with the observed SASA difference. A count of the number of PC, PS, and Chol molecules in the MA shadow further confirmed that this difference was due to the replacement of POPC with Chol (Fig. S9 *E*). Thus, whereas Chol increases headgroup hydration, it decreases the overall bilayer SASA per unit of planar area in the bilayer, as illustrated schematically in Fig. 5 *B*, resulting in a smaller desolvation penalty of the POPC/POPS/Chol membrane upon protein binding. Therefore, our MM-GBSA analysis indicates that Chol both increases the electrostatic attraction between MA and the bilayer, and decreases the cost for headgroup desolvation when the protein binds. These two effects, in concert, result in the energetically more favorable interaction of MA with the +Chol membrane.

The membrane electrostatic potential is a key determinant of MA binding affinity

Although the effects of Chol on membrane thickness and lipid packing are well known (see (54)), the calculations of the previous sections demonstrate that bilayer structural perturbations induced by Chol constitute a general mechanism by which the molecule can indirectly mediate electrostatic interactions with proteins. To further explore retroviral MA-membrane association in the context of these interactions, we used liposome pelleting (25) to measure binding of RSV MA to LUVs with varying POPS and Chol concentrations, and at varying salt concentration. The data were analyzed in terms of calculated electrostatic potential above the membrane surface (Figs. 5 and S10).

Consistent with previous results for RSV and HIV MA and Gag (8,25,38,55), increasing the POPS concentration from 15 to 45 mol % resulted in increased RSV MA binding to LUVs from ~10 to 70% (Fig. 5 *C*, *blue triangles*). A significant enhancement in binding affinity was observed when 36 mol % POPC was replaced with Chol (Fig. 5 *C*, *purple squares*): for example, at 20 mol % POPS, Chol increased MA association with LUVs from 10 to 40%. We also directly tested the ability of Chol to enhance binding

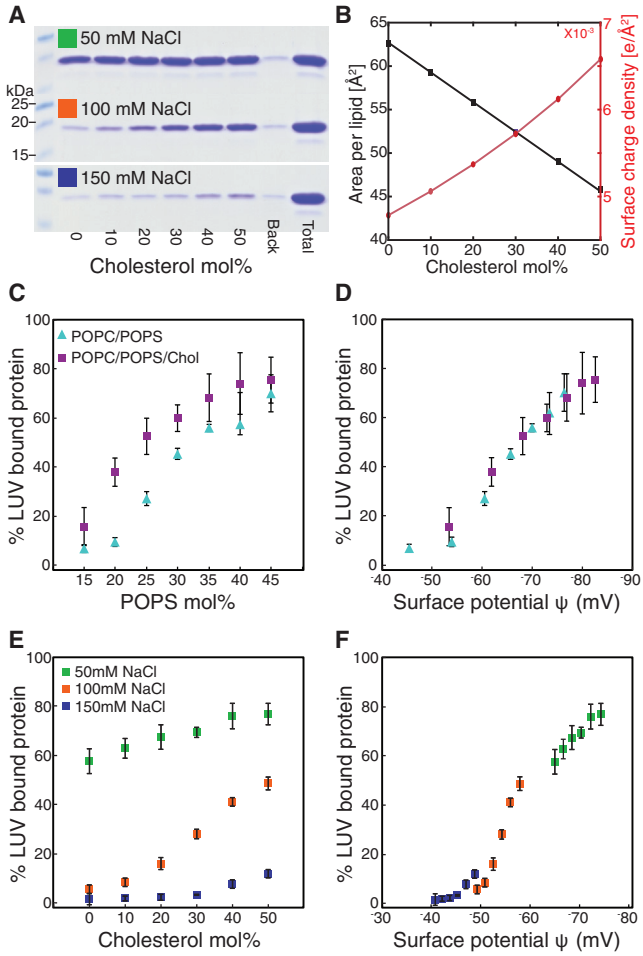

FIGURE 5 RSV MA membrane association is quantitatively explained by membrane surface potential. (*A*) Coomassie-stained gel of pelleted MA associated with LUVs with increasing Chol concentration (0–50 mol %, lanes 2–7). "Back" (lane 8) represents the amount of MA pelleted in the absence of LUVs and "Total" (lane 9) represents the total MA in each binding reaction. (*B*) Calculated membrane surface charge density (*right axis*, *red*) and average area per molecule (*left axis*, *black*) for POPC/POPS/Chol bilayers plotted versus Chol concentration. (*C*) Percent of LUV-bound MA plotted against POPS concentration for membranes without (*light blue triangles*) and with (*purple squares*) 36 mol % Chol. (*D*) Given here is binding data from (*C*) plotted versus calculated ψ. (*E*) Percent of MA bound to LUVs at 30 mol % POPS with increasing Chol and decreasing POPC concentration at different NaCl concentrations: 50 mM (*green*), 100 mM (*orange*), and 150 mM (*blue*). (*F*) Binding data from (*E*) is plotted versus calculated ψ. Legend in (*A*) corresponds to (*A*, *E*, and *F*); legend in (*C*) corresponds to (*C* and *D*). All data points are the average, and error bars are the SD, of no fewer than four independent replicate samples.

under a range of ionic strengths by incrementally replacing POPC with Chol at a fixed POPS concentration of 30 mol %. This replacement decreases the average area per molecule from 62 to 45 Å^2, and increases the surface charge density from 4.8 $\times$ 10^{-3} to 6.6 $\times$ 10^{-3} e$^-$/Å^2 (Fig. 5 *B*). At 100 mM NaCl, we observed a significant increase in the amount of RSV MA associated with LUVs upon increasing Chol concentration (Fig. 5 *E*, *red squares*). Reducing the NaCl concentration to 50 mM resulted in increased binding at all Chol concentrations (Fig. 5 *E*, *green squares*), whereas increasing NaCl concentration to 150 mM practically eliminated binding (Fig. 5 *E*, *blue squares*).

Importantly, the binding trends for all bilayers with and without Chol, and at different ionic strength, collapse onto a single curve when plotted against the electrostatic potential above the membrane surface, ψ, calculated using the Gouy-Chapman model (Fig. 5, *D–F*). In all cases, MA shows little membrane affinity at $\psi > -50$ mV, whereas a dramatic increase in binding occurs as ψ drops to –70 mV. We also observed a similar trend when MA binding was measured as a function of varying NaCl concentration (Fig. S10). Taken together, these results reveal a sigmoidal dependence of binding on membrane surface potential, and demonstrate that the ability of Chol to enhance RSV MA membrane association can be explained by changes in bilayer structure that increase the surface charge density.

Implications for MA binding at the plasma membrane

Fig. 6 *A* shows a model of a mammalian PM taken from published estimates of the outer and inner leaflet lipid composition (5,17,56). Using literature values for individual lipid areas, we calculated the average molecular area (48.9 Å^2) and charge (0.32 e$^-$) for the PM inner leaflet composition (Table S4), which results in an average surface charge density of 6.5×10^{-3} e$^-$/Å^2. It is instructive to consider this charge density in the context of our binding results. Fig. 6 *B* shows a contour plot of ψ as a function of average molecular area and charge at physiological ionic strength (150 mM NaCl) and temperature (37°C), calculated with the Gouy-Chapman model. Also shown is a contour plot of the percentage of membrane-bound MA protein under the same conditions, obtained by mapping the sigmoidal binding curve of Fig. 5 *F* to the calculated surface potential (Fig. S10; Supporting Material). Whereas ψ changes gradually as a function of surface charge density, the fraction of bound protein exhibits large changes over a relatively small range of ψ, from ~–50 to –60 mV. The average PM composition is located approximately at the –50 mV contour, a point that corresponds to weak binding, but that is near the edge of the binding transition. Compositional perturbations such as nonideal mixing that increase the local concentration of charged lipid (corresponding to movement in the $+y$ direction), or increase the local concentration of Chol (corresponding to movement in the $-x$ direction), could therefore act as a binding switch. For example, a 10 Å^2 reduction in the average lipid area—which corresponds to a 10^{-3} e$^-$/Å^2 increase in charge density, or roughly a 20% increase in the local PS density in a patch of average concentration of 30 mol %—could be sufficient to promote electrostatic binding. Thus, by tuning the local lipid composition in the inner leaflet, cells could create binding

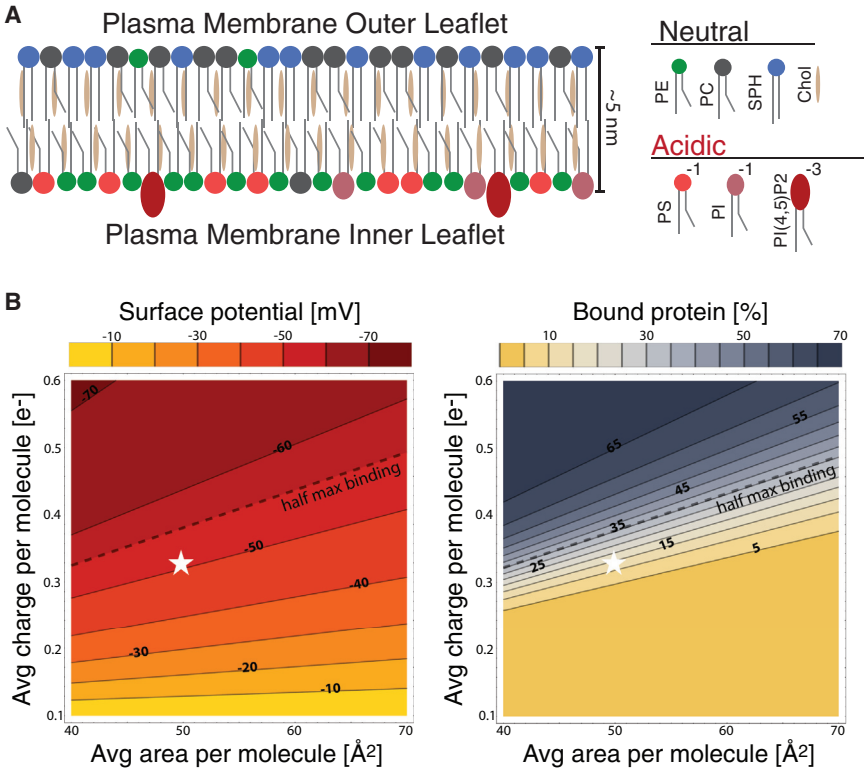

FIGURE 6 Cellular plasma membrane model. (*A*) Asymmetric distribution of PM lipids between the inner (Chol/PE/PC/PS/PI/PIP, 40:28:5:18:8:2 mol %) and outer (Chol/PE/PC/sphingomyelin, 40:7:27:26 mol %) leaflets (see Table S4). (*B*) Contour plots of electrostatic surface potential (*left*) and protein binding (*right*) as a function of average area and charge per molecule. Electrostatic potential was calculated from nonlinear Poisson-Boltzmann theory assuming physiological ionic strength (150 mM NaCl) and temperature (37°C). Protein binding was calculated from a sigmoidal function that maps the binding data displayed in Fig 5 *F* to surface potential (Fig. S10; Supporting Material). The dashed line traces the corresponding contour of half-max binding, and the white star denotes the approximate molecular area (48.9 $Å^2$) and charge (0.32 e^-) of the PM's inner leaflet estimated from the composition given above.

platforms enriched in monovalent charged lipids and Chol, which can attract proteins by means of electrostatic interactions.

The mechanistic insights gained from this study also enable predictions for the effect on protein binding of Chol relative to other lipids. Our results indicate that Chol enhances protein binding through two synergistic effects: it both increases the charge density of the bilayer and decreases the energetic cost of displacing water from the lipid headgroups. As mentioned earlier, the penalty for headgroup desolvation is related to the SASA per unit of planar area. Thus, increasing the membrane's charge density at fixed SASA (for example, by adding PIP2 lipids instead of Chol to a POPC/POPS membrane with a fixed PS mole fraction) should cause a large increase in protein binding. Indeed, this has been shown experimentally for a number of different proteins and model peptides (see Fig. 8 in (25)). On the other hand, decreasing the bilayer's desolvation penalty (or SASA/unit area) at a fixed membrane charge density should result in a smaller increase in binding. One such example can be seen directly in the binding data in Fig. 5 *C*: namely, the –Chol bilayer with 25 mol % PS and the +Chol bilayer with 20 mol % PS have a similar charge density of $\sim 4 \times 10^{-3}$ $e^-/Å^2$, yet the binding to the +Chol bilayer is stronger. This is likely due to Chol's effects on the solvation properties of the membrane. PE lipids, which are abundant in the PM inner leaflet, have smaller headgroups (hence, smaller SASA) and smaller cross-sectional areas than corresponding PC or PS lipids (57). Due to their small SASA and ability to reduce the bilayer area, PE and Chol should have similar effects on binding. Indeed, although at 25 mol % PS, 27% and 53% MA is bound to POPC/POPS and POPC/POPS/Chol bilayers, respectively (Fig. 5 *C*), we find that 58% MA is bound to the corresponding POPE/POPS liposomes under the same conditions.

CONCLUSIONS

We have shown how the interactions crucial for Gag association with the PM can depend on the types of lipids present in the PM inner leaflet. Model membrane studies have previously shown that: 1) electrostatic interactions are critical for MA binding (1,58), 2) cholesterol enhances MA and Gag binding (18,59), and 3) cholesterol condenses the membrane area (60). Our work is the first to explain these observations by describing cholesterol's role using Gouy-Chapman electrostatics. For example, HIV virions are enriched in charged lipids compared to the cellular plasma membrane, and contain 30–40 mol % cholesterol (5), yet many studies of viral protein binding to model membranes do not include cholesterol. Our results suggest that cholesterol enhances MA binding by affecting both the electrostatic and solvation properties of the membrane. Thus, it is an essential component in model membranes, recreating a surface potential and binding conditions representative of the PM inner leaflet.

Moreover, we found that the nonideal mixing behavior of neutral and charged lipids can promote the formation of anionic lipid clusters that act as protein binding sites. We conclude that membranes can mediate nonspecific electrostatic interactions with proteins even in the absence of multivalent acidic lipids, and that bilayer mixing behavior and structural properties should be considered when interpreting protein binding data.

SUPPORTING MATERIAL

Supporting Materials and Methods, thirteen figures, five tables, and two movies are available at http://www.biophysj.org/biophysj/supplemental/S0006-3495(17)30987-6.

AUTHOR CONTRIBUTIONS

M.D., F.A.H., and R.A.D. designed the research, conducted experiments, analyzed data, cowrote the manuscript, and contributed equally to the work. R.L.K. conducted experiments, analyzed data, and cowrote the manuscript. G.K. and M.A.C. performed computational analysis and cowrote the manuscript. G.W.F. and V.M.V. designed the research and cowrote the manuscript. Y.W. conducted experiments. J.K. designed research.

ACKNOWLEDGMENTS

We thank Jany Chan for construction of the expression plasmid and purification of the truncated RSV MA protein used for crystallography; Drew Marquardt and Chris Stanley for technical assistance with SANS measurements; Harel Weinstein for valuable discussions regarding the in silico analysis; Vincent Zoete for providing his implementation of the MM-GBSA free energy decomposition method, which is at the core of the modified version used here; Derek Shore for technical help with the MM-GBSA analysis; and the National Biomedical Center for Advanced ESR Technology at Cornell University and Siddarth Chandrasekaran for help with ESR data collection and analysis.

This work was supported by National Institutes of Health (NIH) grant R01GM107013 (to V.M.V.), National Institutes of Health (NIH) grant R01GM105684 (to G.W.F.), and National Institutes of Health (NIH) grant PO1DA012408 (for M.D., G.K., and M.A.C.). The work at Oak Ridge National Laboratory's EQ-SANS instrument at the Spallation Neutron Source was sponsored by the Basic Energy Science (BES) Program, Office of Science, US Department of Energy (DOE) under contract no. DEAC05-00OR22725 with UT-Battelle. J.K. is supported through the Scientific User Facilities Division of the Department of Energy (DOE) Office of Science.

REFERENCES

1. Dick, R. A., and V. M. Vogt. 2014. Membrane interaction of retroviral Gag proteins. *Front. Microbiol.* 5:187.
2. Ono, A., and E. O. Freed. 2001. Plasma membrane rafts play a critical role in HIV-1 assembly and release. *Proc. Natl. Acad. Sci. USA.* 98:13925–13930.
3. Brügger, B., B. Glass, …, H. G. Kräusslich. 2006. The HIV lipidome: a raft with an unusual composition. *Proc. Natl. Acad. Sci. USA.* 103:2641–2646.
4. Chan, R., P. D. Uchil, …, M. R. Wenk. 2008. Retroviruses human immunodeficiency virus and murine leukemia virus are enriched in phosphoinositides. *J. Virol.* 82:11228–11238.
5. Lorizate, M., T. Sachsenheimer, …, B. Brügger. 2013. Comparative lipidomics analysis of HIV-1 particles and their producer cell membrane in different cell lines. *Cell. Microbiol.* 15:292–304.
6. Krementsov, D. N., P. Rassam, …, M. Thali. 2010. HIV-1 assembly differentially alters dynamics and partitioning of tetraspanins and raft components. *Traffic.* 11:1401–1414.
7. Nanda, H., S. A. Datta, …, J. E. Curtis. 2010. Electrostatic interactions and binding orientation of HIV-1 matrix studied by neutron reflectivity. *Biophys. J.* 99:2516–2524.
8. Dick, R. A., S. A. Datta, …, V. M. Vogt. 2015. Hydrodynamic and membrane binding properties of purified Rous sarcoma virus Gag protein. *J. Virol.* 89:10371–10382.
9. Datta, S. A., F. Heinrich, …, H. Nanda. 2011. HIV-1 Gag extension: conformational changes require simultaneous interaction with membrane and nucleic acid. *J. Mol. Biol.* 406:205–214.
10. Machán, R., and M. Hof. 2010. Recent developments in fluorescence correlation spectroscopy for diffusion measurements in planar lipid membranes. *Int. J. Mol. Sci.* 11:427–457.
11. Goksu, E. I., and M. L. Longo. 2010. Ternary lipid bilayers containing cholesterol in a high curvature silica xerogel environment. *Langmuir.* 26:8614–8624.
12. Heberle, F. A., R. S. Petruzielo, …, J. Katsaras. 2013. Bilayer thickness mismatch controls domain size in model membranes. *J. Am. Chem. Soc.* 135:6853–6859.
13. Marquardt, D., F. A. Heberle, …, J. Katsaras. 2015. On scattered waves and lipid domains: detecting membrane rafts with x-rays and neutrons. *Soft Matter.* 11:9055–9072.
14. Pencer, J., S. Krueger, …, J. Katsaras. 2006. Method of separated form factors for polydisperse vesicles. *J. Appl. Cryst.* 39:293–303.
15. Kucerka, N., J. F. Nagle, …, J. Katsaras. 2008. Lipid bilayer structure determined by the simultaneous analysis of neutron and x-ray scattering data. *Biophys. J.* 95:2356–2367.
16. Charlier, L., M. Louet, …, N. Floquet. 2014. Coarse-grained simulations of the HIV-1 matrix protein anchoring: revisiting its assembly on membrane domains. *Biophys. J.* 106:577–585.
17. van Meer, G., D. R. Voelker, and G. W. Feigenson. 2008. Membrane lipids: where they are and how they behave. *Nat. Rev. Mol. Cell Biol.* 9:112–124.
18. Dick, R. A., S. L. Goh, …, V. M. Vogt. 2012. HIV-1 Gag protein can sense the cholesterol and acyl chain environment in model membranes. *Proc. Natl. Acad. Sci. USA.* 109:18761–18766.
19. Nezil, F. A., and M. Bloom. 1992. Combined influence of cholesterol and synthetic amphiphilic peptides upon bilayer thickness in model membranes. *Biophys. J.* 61:1176–1183.
20. Kucerka, N., J. D. Perlmutter, …, J. N. Sachs. 2008. The effect of cholesterol on short- and long-chain monounsaturated lipid bilayers as determined by molecular dynamics simulations and x-ray scattering. *Biophys. J.* 95:2792–2805.
21. McIntosh, T. J., A. D. Magid, and S. A. Simon. 1989. Cholesterol modifies the short-range repulsive interactions between phosphatidylcholine membranes. *Biochemistry.* 28:17–25.
22. Subczynski, W. K., A. Wisniewska, …, A. Kusumi. 1994. Hydrophobic barriers of lipid bilayer membranes formed by reduction of water penetration by alkyl chain unsaturation and cholesterol. *Biochemistry.* 33:7670–7681.
23. Simon, S. A., T. J. McIntosh, and R. Latorre. 1982. Influence of cholesterol on water penetration into bilayers. *Science.* 216:65–67.
24. Kingsley, P. B., and G. W. Feigenson. 1979. Synthesis of a perdeuterated phospholipid—1,2-dimyristoyl-*sn*-glycero-3-phosphocholine-D72. *Chem. Phys. Lipids.* 24:135–147.
25. Wen, Y., R. A. Dick, …, V. M. Vogt. 2016. Effects of membrane charge and order on membrane binding of the retroviral structural protein Gag. *J. Virol.* 90:9518–9532.
26. Arnold, O., J. C. Bilheux, …, J. Zikoysky. 2014. Mantid—data analysis and visualization package for neutron scattering and mu SR experiments. *Nucl. Instrum. Meth. A.* 764:156–166.

27. Heberle, F. A., V. N. P. Anghel, and J. Katsaras. 2015. Scattering from phase-separated vesicles. I. An analytical form factor for multiple static domains. *J. Appl. Cryst.* 48:1391–1404.

28. Kučerka, N., J. F. Nagle, …, P. Balgavý. 2004. Models to analyze small-angle neutron scattering from unilamellar lipid vesicles. *Phys. Rev. E Stat. Nonlin. Soft Matter Phys.* 69:051903.

29. McDonnell, J. M., D. Fushman, …, D. Cowburn. 1998. Solution structure and dynamics of the bioactive retroviral M domain from Rous sarcoma virus. *J. Mol. Biol.* 279:921–928.

30. Andrec, M., D. A. Snyder, …, R. M. Levy. 2007. A large data set comparison of protein structures determined by crystallography and NMR: statistical test for structural differences and the effect of crystal packing. *Proteins.* 69:449–465.

31. Nelle, T. D., and J. W. Wills. 1996. A large region within the Rous sarcoma virus matrix protein is dispensable for budding and infectivity. *J. Virol.* 70:2269–2276.

32. Dick, R. A., M. Barros, …, V. M. Vogt. 2015. Membrane binding of the Rous sarcoma virus Gag protein is cooperative and dependent on the spacer peptide assembly domain. *J. Virol.* 90:2473–2485.

33. Phillips, J. C., R. Braun, …, K. Schulten. 2005. Scalable molecular dynamics with NAMD. *J. Comput. Chem.* 26:1781–1802.

34. Best, R. B., X. Zhu, …, A. D. MacKerell, Jr. 2012. Optimization of the additive CHARMM all-atom protein force field targeting improved sampling of the backbone φ, ψ and side-chain $\chi(1)$ and $\chi(2)$ dihedral angles. *J. Chem. Theory Comput.* 8:3257–3273.

35. Klauda, J. B., R. M. Venable, …, R. W. Pastor. 2010. Update of the CHARMM all-atom additive force field for lipids: validation on six lipid types. *J. Phys. Chem. B.* 114:7830–7843.

36. Venable, R. M., F. L. Brown, and R. W. Pastor. 2015. Mechanical properties of lipid bilayers from molecular dynamics simulation. *Chem. Phys. Lipids.* 192:60–74.

37. Doktorova, M., D. Harries, and G. Khelashvili. 2017. Determination of bending rigidity and tilt modulus of lipid membranes from real-space fluctuation analysis of molecular dynamics simulations. *Phys. Chem. Chem. Phys.* 19:16806–16818.

38. Dalton, A. K., P. S. Murray, …, V. M. Vogt. 2005. Biochemical characterization of Rous sarcoma virus MA protein interaction with membranes. *J. Virol.* 79:6227–6238.

39. Kučerka, N., M. P. Nieh, and J. Katsaras. 2011. Fluid phase lipid areas and bilayer thicknesses of commonly used phosphatidylcholines as a function of temperature. *Biochim. Biophys. Acta.* 1808:2761–2771.

40. Pan, J., X. Cheng, …, J. Katsaras. 2014. The molecular structure of a phosphatidylserine bilayer determined by scattering and molecular dynamics simulations. *Soft Matter.* 10:3716–3725.

41. Kučerka, N., J. Pencer, …, J. Katsaras. 2007. Influence of cholesterol on the bilayer properties of monounsaturated phosphatidylcholine unilamellar vesicles. *Eur. Phys. J. E Soft Matter.* 23:247–254.

42. Heberle, F. A., and G. W. Feigenson. 2011. Phase separation in lipid membranes. *Cold Spring Harb. Perspect. Biol.* 3:a004630.

43. Almeida, P. F. 2009. Thermodynamics of lipid interactions in complex bilayers. *Biochim. Biophys. Acta.* 1788:72–85.

44. Huang, J., J. E. Swanson, …, G. W. Feigenson. 1993. Nonideal mixing of phosphatidylserine and phosphatidylcholine in the fluid lamellar phase. *Biophys. J.* 64:413–425.

45. Khelashvili, G., and D. Harries. 2010. Modeling signaling processes across cellular membranes using a mesoscopic approach. *Annu. Rep. Comput. Chem.* 6:236–261.

46. Khelashvili, G., H. Weinstein, and D. Harries. 2008. Protein diffusion on charged membranes: a dynamic mean-field model describes time evolution and lipid reorganization. *Biophys. J.* 94:2580–2597.

47. Callahan, E. M., and J. W. Wills. 2000. Repositioning basic residues in the M domain of the Rous sarcoma virus gag protein. *J. Virol.* 74:11222–11229.

48. Andelman, D. 2006. Introduction to electrostatics in soft and biological matter. *In* Soft Condensed Matter Physics in Molecular and Cell Biology. W. C. K. Poon and D. Andelman, eds. Taylor & Francis, Abingdon, United Kingdom, pp. 97–122.

49. Jo, S., T. Kim, …, W. Im. 2008. CHARMM-GUI: a web-based graphical user interface for CHARMM. *J. Comput. Chem.* 29:1859–1865.

50. Huang, J., and G. W. Feigenson. 1993. Monte Carlo simulation of lipid mixtures: finding phase separation. *Biophys. J.* 65:1788–1794.

51. Srinivasan, J., M. W. Trevathan, …, D. A. Case. 1999. Application of a pairwise generalized Born model to proteins and nucleic acids: inclusion of salt effects. *Theor. Chem. Acc.* 101:426–434.

52. Gohlke, H., C. Kiel, and D. A. Case. 2003. Insights into protein-protein binding by binding free energy calculation and free energy decomposition for the Ras-Raf and Ras-RalGDS complexes. *J. Mol. Biol.* 330:891–913.

53. Zoete, V., M. Meuwly, and M. Karplus. 2005. Study of the insulin dimerization: binding free energy calculations and per-residue free energy decomposition. *Proteins.* 61:79–93.

54. Pan, J., S. Tristram-Nagle, and J. F. Nagle. 2009. Effect of cholesterol on structural and mechanical properties of membranes depends on lipid chain saturation. *Phys. Rev. E Stat. Nonlin. Soft Matter Phys.* 80:021931.

55. Dalton, A. K., D. Ako-Adjei, …, V. M. Vogt. 2007. Electrostatic interactions drive membrane association of the human immunodeficiency virus type 1 Gag MA domain. *J. Virol.* 81:6434–6445.

56. Murate, M., and T. Kobayashi. 2016. Revisiting transbilayer distribution of lipids in the plasma membrane. *Chem. Phys. Lipids.* 194:58–71.

57. Kučerka, N., B. van Oosten, …, J. Katsaras. 2015. Molecular structures of fluid phosphatidylethanolamine bilayers obtained from simulation-to-experiment comparisons and experimental scattering density profiles. *J. Phys. Chem. B.* 119:1947–1956.

58. Murray, P. S., Z. Li, …, D. Murray. 2005. Retroviral matrix domains share electrostatic homology: models for membrane binding function throughout the viral life cycle. *Structure.* 13:1521–1531.

59. Barros, M., F. Heinrich, …, M. Lösche. 2016. Membrane binding of HIV-1 matrix protein: dependence on bilayer composition and protein lipidation. *J. Virol.* 90:4544–4555.

60. Heftberger, P., B. Kollmitzer, …, G. Pabst. 2015. In situ determination of structure and fluctuations of coexisting fluid membrane domains. *Biophys. J.* 108:854–862.

Biophysical Journal, Volume *113*

Supplemental Information

Cholesterol Promotes Protein Binding by Affecting Membrane Electrostatics and Solvation Properties

Milka Doktorova, Frederick A. Heberle, Richard L. Kingston, George Khelashvili, Michel A. Cuendet, Yi Wen, John Katsaras, Gerald W. Feigenson, Volker M. Vogt, and Robert A. Dick

Supporting Material for:

Cholesterol promotes binding of retroviral matrix protein by indirectly affecting membrane electrostatics and solvation properties

Milka Doktorova,[1,#] Frederick A. Heberle,[2-4, *,#] Richard L. Kingston,[5] George Khelashvili,[6] Michel A. Cuendet,[6] Yi Wen,[7] John Katsaras,[2,4,8,9] Gerald W. Feigenson,[7] Volker M. Vogt,[7] and Robert A. Dick[7, *,#]

[1]Tri-Institutional PhD Program in Computational Biology and Medicine, Weill Cornell Medical College, New York, New York 10065, United States; [2]The Bredesen Center for Interdisciplinary Research and Graduate Education, University of Tennessee, Knoxville, Tennessee 37996, United States; [3]Joint Institute for Biological Sciences, Oak Ridge National Laboratory, Oak Ridge, Tennessee 37831, United States; [4]Biology and Soft Matter Division, Oak Ridge National Laboratory, Oak Ridge, Tennessee 37831, United States; [5]School of Biological Sciences, The University of Auckland, Auckland, New Zealand; [6]Department of Physiology and Biophysics, Weill Cornell Medical College, New York, New York 10065, United States; [7]Department of Biochemistry and Molecular Cell Biology, Cornell University, Ithaca, New York 14853, United States; [8]Department of Physics and Astronomy, University of Tennessee, Knoxville, Tennessee 37996, United States; [9]Shull Wollan Center, Oak Ridge National Laboratory, Oak Ridge, Tennessee 37831, United States;

[#]Contributed equally
[*]Co-corresponding authors

DETAILED METHODS

SANS data analysis. SANS data were modeled with a heterogeneous core-shell (HCS) form factor (1) with modifications discussed here. This model is appropriate for describing scattering from a "patchy" spherical shell particle, such as a phase-separated or protein-bound unilamellar lipid bilayer vesicle, shown schematically in Fig. S2A. The coherent scattered intensity of such a particle contains three contributions:

$$I(q) = I_{hom}(q) + I_{intra}(q) + I_{inter}(q). \qquad (S1)$$

The first term in Eq. S1 accounts for the *homogeneous* contribution to the total scattering arising from structure normal to the plane of the bilayer. Differences in the atomic composition of lipid headgroups and chains generally results in different average neutron scattering length densities (NSLDs) for these layers, with the NSLD variation along the bilayer normal described quantitatively by a radial NSLD profile $\rho(r)$, where r is the radial distance from the center of a vesicle. In a phase-separated vesicle with two coexisting environments, the transverse structure from each phase contributes to the homogeneous scattering, which can be expressed as:

$$I_{hom}(q) = 4\pi\left[2\sqrt{\pi}M_0(q) + 2\sqrt{\pi}a_d W_0(q)\right]^2, \qquad (S2)$$

$$M_0(q) = \int_0^\infty [\rho_c(r) - \rho_s] r^2 j_0(qr) dr, \qquad (S3)$$

$$W_0(q) = \int_0^\infty [\rho_d(r) - \rho_c(r)] r^2 j_0(qr) dr. \qquad (S4)$$

Here, ρ_d, ρ_c, and ρ_s refer respectively to the NSLD of the domain phase, continuous phase, and surrounding aqueous solvent, a_d is the fraction of the vesicle surface area occupied by the domain phase, and j_0 is the zeroth order Bessel function. From Eqs. S2-4, it is clear that I_{hom} depends only on the radial (transverse) bilayer structure and relative amounts of the two phases, but not on the size or spatial organization of domains. The latter information is accounted for by the second and third terms in Eq. S1, I_{intra} and I_{inter}. Making use of a spherical harmonic expansion of the vesicle scattering amplitude, the intradomain scattering contribution is given by:

$$I_{intra}(q) = 4\pi N_d \sum_{l=1}^{\infty} \left|\widetilde{w}_l^0(\alpha_d)\right|^2 |W_l(q)|^2, \qquad (S5)$$

$$W_l(q) = \int_0^\infty [\rho_d(r) - \rho_c(r)] r^2 j_l(qr) dr, \qquad (S6)$$

$$\widetilde{w}_l^0(\alpha_d) = \frac{\sqrt{(2l+1)}}{2l}[\cos\alpha_d\, P_l(\cos\alpha_d) - P_{l+1}(\cos\alpha_d)], \qquad (S7)$$

where N_d is the number of domains, α_d is the angle formed by vectors pointing from the vesicle center to the domain center and edge, and P_l is the Legendre polynomial of degree l. Finally, the interdomain scattering arising from coherent interference between different domains is given by:

$$I_{inter}(q) = 4\pi \sum_{J \neq K} \sum_{l=1}^{\infty} \left|\widetilde{w}_l^0(\alpha_d)\right|^2 |W_l(q)|^2 P_l\left(\cos\theta_{JK}\right), \qquad (S8)$$

where θ_{JK} is the angle between the vesicle center and the centers of domains J and K. The effects of vesicle size polydispersity are included by averaging the monodisperse intensity $I(q, R)$ (i.e., Eqs. S1-8) over a Schulz distribution:

$$G(R) = \left(\frac{1}{R_m \sigma^2}\right)^{(1/\sigma^2)} \frac{R^{(1/\sigma^2 - 1)}}{\Gamma(1/\sigma^2)} exp\left[\frac{-R}{R_m \sigma^2}\right], \qquad (S9)$$

where R_m is the most probable vesicle radius, σ is the root mean square deviation from R_m, and Γ is the gamma function. The polydisperse intensity $I_P(q)$ is then given by:

$$I_P(q) = \int_0^{\infty} I(q, R) G(R) dR. \qquad (S10)$$

To summarize, the HCS model requires as input:

1. Radial SLD profiles for the domain and continuous phases, $\rho_d(r)$ and $\rho_c(r)$. Assuming that the radial bilayer structure does not depend on vesicle size R, then $\rho(r; R) = \rho(z + R)$ for all R, where $\rho_d(z)$ and $\rho_c(z)$ are transverse SLD profiles centered at $z = 0$. Diverse models for transverse SLD profiles can be found in the literature (reviewed in (2)); our analysis used a simple "slab" model described below.
2. The size and spatial arrangement of domains on the vesicle surface, given by the angle α_d and the distribution of domain center-center angles θ_{JK}. Our analysis assumed circular domains with a fixed area of 1375 Å^2 (corresponding to the cross-sectional area of an MA monomer), randomly arranged on the vesicle surface.
3. A vesicle size distribution $G(R; R_m, \sigma)$. We note that for vesicles larger than ~ 300 Å diameter, the precise values of R_m and σ do not affect $I(q)$ for q > 0.05 Å^{-1}. In our analysis, we fixed these parameters at 500 Å and 125 Å, respectively (i.e., a relative polydispersity of 0.25).

Transverse bilayer structure was modeled for each phase separately, using volume probability distributions for different lipid and protein "quasi-molecular fragments". The lipid headgroups and hydrocarbon chains were modeled as separate fragments with uniform probability distributions:

$$P_i(z) = \frac{N_i V_i}{A_L \sigma_i}[\Theta(\mathrm{z} - \mathrm{z}_i) - \Theta(\mathrm{z} - \mathrm{z}_i - \sigma_i)], \qquad (S11)$$

$$\Theta(x) = \begin{cases} 0, & x < 0 \\ 1, & x \geq 0 \end{cases}, \qquad (S12)$$

where V_i is the fragment volume, σ_i is the fragment width along the bilayer normal, A_L is the unit cell area, z_i is the fragment's lower boundary ($z_i + \sigma_i$ is the upper boundary), and Θ is the unit step function. For the domain phase, externally-bound protein was modeled with a Gaussian probability distribution:

$$P_P(z) = \frac{2\chi_P V_P}{\sqrt{2\pi} A_L \sigma_p} exp\left[\frac{-(z - z_p)^2}{2{\sigma_p}^2}\right]. \qquad (S13)$$

In Eq. S13, χ_P is the protein mole fraction in the protein+lipid sample; because the bilayer unit cell by definition contains exactly two lipids, the (fractional) number of proteins per unit cell is given by $N_P = 2\chi_P$. All lipid and protein fragment volume probability functions satisfy the following relationships:

$$\int P_i(z)dz = \frac{N_i V_i}{A_L}, \qquad (S14)$$

$$P(z) = \sum_i P_i(z) + P_w(z) = 1, \qquad (S15)$$

where N_i is the number of fragment i contained in the unit cell, P_w is the water probability, and P is the total probability. These equations enforce local volume conservation: any volume not occupied by a lipid or protein fragment must be occupied by water. Equation S15 can be rearranged to define the water probability function in terms of lipid and protein fragment probabilities:

$$P_w(z) = 1 - \sum_i P_i(z). \qquad (S16)$$

The scattering length density profile is then given by a weighted sum of the lipid and protein fragment probabilities:

$$\rho(z) = \sum_i \rho_i P_i(z), \qquad (S17)$$

$$\rho_i = \frac{b_i}{V_i}, \qquad (S18)$$

where b_i is the fragment's coherent scattering length. In the case of mixtures of two or more lipids, the lipid fragments are composites whose properties represent average properties of the mixture, and are approximated as mole fraction-weighted sums of individual lipid properties, i.e.:

$$V_i = \sum_j \chi_j V_{ij}, \qquad (S19)$$

$$b_i = \sum_j \chi_j b_{ij}, \qquad (S20)$$

where V_{ij} and b_{ij} are the fragment i volume and scattering length of mixture component j, respectively, and χ_j is the component j mole fraction. Values for the volumes and scattering length densities of the different lipid and protein species are given in Table S3. The total bilayer (Luzzati) thickness D_B is calculated from the total lipid volume V_L and area per lipid:

$$D_B = V_L/A_L, \qquad (S21)$$

where V_C and V_H are the lipid chain and headgroup volumes, respectively, and $V_L = V_C + V_H$. Similarly, the hydrocarbon chain thickness $2D_C$ is calculated from the hydrocarbon chain volume and area per lipid:

$$2D_C = 2V_C/A_L. \qquad (S22)$$

Finally, to account for the smearing effects of thermal disorder, the NSLD profile was smoothed by convolution with a Gaussian function:

$$\tilde{\rho}(z) = \rho * g = \int_{-\infty}^{\infty} \rho(x) g(\sigma_s; z - x) dx, \qquad (S23)$$

with the width of the smoothing window σ_s fixed at 2 Å.

X-ray crystallography. All crystals were grown using the sitting-drop vapor diffusion technique. Crystallization conditions were identified using screening experiments based on orthogonal arrays (3). Details are given in Table S1. Prior to data collection crystals were transferred into cryo-protective solutions, and vitrified by direct immersion in liquid nitrogen. Diffraction data were collected by the oscillation method, using both laboratory and synchrotron radiation sources (Table S1), with crystals maintained at 100–110 K in a cold gas stream throughout. Data integration and scaling were performed with the program HKL2000 (4).

The structure of RSV MA was determined by the method of Multiple Isomorphous Replacement with Anomalous Scattering (MIRAS). To produce isomorphous derivatives, the crystals were soaked for 2-10 minutes in cryo-protective solutions incorporating either 1 M NaI or 1 M NaBr, prior to immersion in liquid nitrogen. Diffraction data on NaBr-soaked crystals were collected at several wavelengths near the Bromine K edge, while diffraction data on NaI-soaked crystals were collected at wavelengths of 1.033 and 1.653 Å. The program SHELXD (5) was used to identify the halide-binding sites. The NaI and NaBr-derivatized crystals shared a common site, with an additional unique site

for the NaI derivative. The program SHARP 2.0 (6) was used to refine site occupancies and calculate phases, producing a partially interpretable electron density map in which helices were clearly visible. Repeat rounds of model building and refinement using the programs Coot (7) and Refmac (8) allowed for the completion of a structural model for the N-terminal region of the molecule (amino acids 1-102). There was no interpretable electron density associated with the remainder of the sequence (amino acids 103-155). Subsequently structures of a truncated variant (MA2-102) were determined by the method of molecular replacement, using the program Phaser (9) to position the structural model where required. Statistics associated with the native data sets and refined structural models are shown in Table S1.

MD simulations. All MD simulations were performed with the NAMD software, versions 2.7-2.10 (10) and analyzed with VMD (11) and custom Tcl scripts. Protein secondary structure was calculated using DSSP (12).

The two bilayers, POPC/POPS 70/30 mol% and POPC/POPS/Chol 34/30/36 mol%, were constructed with CHARMM-GUI (13) and simulated as described in (14). The bilayers contained 70 and 100 lipids per leaflet, respectively, and were solvated with 45 waters/lipid and 50 mM NaCl. The POPC/POPS bilayer was simulated for a total of 191 ns and the POPC/POPS/Chol bilayer for a total of 270 ns. The last 100 ns of each simulation were used for subsequent analysis.

MA was placed on top of each bilayer using coordinates taken from the last frames of the two bilayer-only simulations. MA was oriented with respect to the membrane surface as previously done (15). The systems were energy minimized for 24000 steps and run for 1.2 ns with a 1 fs time step before the production runs. Three replica simulations were run for the POPC/POPS +MA system with total simulation times of 184 ns, 242 ns and 198 ns. The POPC/POPS/Chol +MA system was simulated for 74 ns, after which time two replica simulations were started and run for an additional 132 and 141 ns respectively. The last 100 ns of the trajectories were used for subsequent analysis.

To ensure that the applied periodic boundary conditions did not affect the interaction of the protein with the bilayer, an additional simulation was performed in which two MA proteins were placed as described above, but on each side of a POPC/POPS/Chol bilayer (i.e., one on the top leaflet and one on the bottom leaflet). Thus, any modes of interaction that could cause large leaflet deformations and accumulation of pressure if applied only on one side of the bilayer, would be counterbalanced and not suppressed. The simulation was run for a total of 204 ns and the interaction of each of the two MA proteins with their respective leaflets was analyzed separately. Since the results were the same as in the systems with a single MA, they were treated as two additional replicas of the POPC/POPS/Chol +MA system and were analyzed jointly with the other simulations.

Calculations of electrostatic potential and fraction of bound protein. The electrostatic potential on the membrane surface was calculated using the analytical solution to the non-linear Poisson-Boltzmann equation (Eq. 15 in (16)) with the membrane surface taken as $z = 0$. Surface charge density was calculated as the mole fraction of charge divided by

the average area per lipid of the bilayer, with units of $e^-/Å^2$. Unless otherwise noted, the areas per lipid calculated from MD simulations were used.

To generate the contour plots in Fig. 6B of the main text, the fraction of bound protein f from protein binding assays (i.e., the data in Fig. 5F of the main text) was modeled as a sigmoidal function of the membrane surface potential ψ:

$$f(\psi) = \frac{a}{1 + e^{b(\psi - \psi^*)}}, \qquad (S24)$$

where a is a scaling factor representing the maximum bound fraction, b is a stretching factor representing the width of the sigmoidal binding transition, and ψ^* is the surface potential at half-maximum binding. The three adjustable parameters were optimized with Mathematica's built-in NonlinearModelFit function using a Levenberg-Marquardt algorithm. The best-fit parameter values were: a = 70.9%, b = 0.285, and ψ^* = –55.9 mV (Fig. S10). This parameter set was used with Eq. S24 to map the calculated membrane surface potential (Fig. 6B, left-hand plot) to the percentage of bound protein, generating the right-hand plot in Fig. 6B (main text).

Monte Carlo simulations of equilibrium lipid distributions. Monte Carlo simulations of a 100 × 100 triangular lattice in the canonical ensemble were performed using custom code written in Mathematica and available from the authors upon request. Each lattice site represented either a PC or PS lipid, with the composition fixed at 70/30 mol% PC/PS. Neglecting multibody and long-range electrostatic interactions, the total energy of a lattice composed of a fixed number of PS and PC lipids (N_{PS} and N_{PC}, respectively) is given by the sum of unique nearest-neighbor pairwise interactions (17):

$$U^T = \frac{ZN_{PS}U_{PS-PS}}{2} + \frac{ZN_{PC}U_{PC-PC}}{2} + N_{PS-PC}\Delta E_m, \qquad (S25)$$

$$\Delta E_m = U_{PS-PC} - (U_{PS-PS} + U_{PC-PC})/2, \qquad (S26)$$

where U_{PS-PS} and U_{PC-PC} are the interaction energies for a neighboring pair of PS and PC lipids, respectively, N_{PS-PC} is the total number of PC/PS contacts, and Z is the number of nearest neighbors in a lattice site (6 for a triangular lattice). The sole adjustable parameter ΔE_m is the excess mixing energy of a PC/PS pair. The first two terms in Eq. S25 do not depend on the lipid distribution and therefore do not contribute to non-ideal mixing. As a result, only the third term was updated. For each proposed update, the position of two randomly chosen lipids was exchanged, generating a change in the lattice energy $\Delta U^T \equiv U^T_{new} - U^T_{init}$ that was either favorable/neutral ($\Delta U^T \leq 0$) or unfavorable ($\Delta U^T > 0$). Importance sampling was based on the Metropolis criterion, whereby a favorable move was always accepted, and an unfavorable move was accepted with probability $P = \exp(-\Delta U^T / k_B T)$ by first drawing a random number R from a uniform probability distribution $R \sim U[0,1]$ and then performing the exchange if $R \leq P$. Each simulation was equilibrated for a minimum of 10^3 MC cycles, where a cycle is defined as a number of proposed exchanges equal to the lattice size (here, 10^4

exchanges). Equilibrium was judged by convergence of the lattice energy upon starting from either (a) a completely random distribution of the lipids, or (b) a block distribution of the lipids. The number of MC cycles required to reach convergence increased with increasing ΔE_m, varying from ~ 300 cycles for ΔE_m = + 0.1 k_BT to ~ 10^4 cycles for ΔE_m = + 0.5 k_BT. For additional details on MC lattice simulations, we point the reader toward several studies relevant to lipid bilayers (17-27).

Calculation of relative surface potential from Monte Carlo snapshots. To calculate a surface potential map from MC snapshots, lattice sites were assigned relative real space coordinates $\boldsymbol{l} = (l_x, l_y, 0)$ using the relationship between the triangular lattice spacing λ and the unit cell area A:

$$\lambda = \left(\frac{2A}{\sqrt{3}}\right)^{1/2}, \qquad (S27)$$

and taking A to be the area per lipid (63 Å^2). The potential V at an arbitrary point $\boldsymbol{p} = (p_x, p_y, p_z)$ is then given by:

$$V = k_e \sum_j \frac{q_j}{r_j}, \qquad (S28)$$

where k_e is Coulomb's constant, $r_j = \|\boldsymbol{l_j} - \boldsymbol{p}\|$ is the distance between point $\boldsymbol{p}$ and lattice site j, q_j is the charge at lattice site j (i.e., 0 for a neutral PC lipid and the elementary charge e^- for an acidic PS lipid), and the sum is over all lattice sites j. Because the absolute potential depends strongly on the lattice size, V was normalized to a reference potential $\bar{v}$ arising from a uniformly charged lattice calculated as:

$$\bar{v} = k_e \chi e^- \sum_j r_j^{-1}, \qquad (S29)$$

where χ is the mole fraction of charged lipid in the mixture (here, 0.3). Finally the relative potential $\tilde{V}$ at point $\boldsymbol{p}$ was calculated as $\tilde{V} = V/\bar{v}$.

MM/GBSA calculations. The molecular mechanics-generalized Born and surface area (MM-GBSA) method (28, 29) is a so-called end-point free energy approach to estimate the binding free energy between two molecular binding partners, based on a sample of molecular conformations of the complex generated by all-atom molecular dynamics simulation. The MM-GBSA method has been used successfully to estimate the binding free energy of ligands to proteins, and to calculate single-residue contributions to binding free energies of large protein-protein complexes (28-30). For each trajectory frame, the solvent and ions are stripped away and only the coordinates of the binding partners are kept. In the one-trajectory MM-GBSA approach employed here, coordinates for each partner in isolation are extracted from the same trajectory frames of the complex, assuming that these are also acceptable conformations for the molecules in solution. As in

the preceding molecular mechanics-Poisson Boltzmann surface area (MM-PBSA) method (31), the solvation effects are approximated by immersing the molecules in a continuous medium with high relative dielectric constant $\varepsilon_r^{\mathrm{solv}} = 80$. Following the thermodynamic cycle shown in Fig. S11, the binding free energy between two binding partners, here membrane (M) and protein (P), is expressed as

$$\Delta G_{\mathrm{bind}} = \Delta E_{\mathrm{int}}^{\mathrm{vac}} + \Delta G_{\mathrm{desolv}}(M) + \Delta G_{\mathrm{desolv}}(P) - \Delta G_{\mathrm{desolv}}(MP) + \Delta S_{\mathrm{bind}}^{\mathrm{vib}} . \qquad (S30)$$

In general, $\Delta E_{\mathrm{int}}^{\mathrm{vac}}$ is the difference in internal bonded and non-bonded energies in M and P upon binding, calculated with the same Charmm36 parameters (32) as in the MD simulation. Here, a lot of terms cancel out since we use the same coordinates for bound and unbound molecules, such that $\Delta E_{\mathrm{int}}^{\mathrm{vac}}$ boils down to the Van der Waals and electrostatic interaction energies between M and P. $\Delta S_{\mathrm{bind}}^{\mathrm{vib}}$ is the difference in internal vibrational entropy upon binding, which we neglect in the present application. The desolvation penalty for molecular system X is composed of a polar and a non-polar term,

$$\Delta G_{\mathrm{desolv}}(X) = \Delta G_{\mathrm{P,desolv}}(X) + \Delta G_{\mathrm{NP,desolv}}(X). \qquad (S31)$$

The non-polar term accounts for energetic and entropic effects in the solvent related to creating the cavity occupied by X. This term is simply proportional to the SASA,

$$\Delta G_{\mathrm{NP,desolv}}(X) = \gamma\, SASA(X), \qquad (S32)$$

with $\gamma = -0.0072$ kcal/mol/Å^2 (33). The SASA is calculated by rolling a virtual 1.4 Å radius ball over the molecules. The polar solvation term is calculated using the generalized Born (GB) equation (28, 31) with an additional Debeye-Hückel correction to account for ionic screening (28):

$$\Delta G_{\mathrm{P,desolv}}(X) = \frac{c}{2}\left(\frac{1}{\varepsilon_r^{\mathrm{vac}}} - \frac{e^{-\kappa r_{ij}^{\mathrm{GB}}}}{\varepsilon_r^{\mathrm{solv}}}\right)\sum_{i,j\in X}\frac{q_i q_j}{r_{ij}^{\mathrm{GB}}} . \qquad (S33)$$

Here, the q_i are atomic partial charges, $c = 332.0672$ kcal/mol Å / u^2, and κ is the Debeye-Hückel screening constant expressed in Å^{-1} as $\kappa = 0.316\sqrt{[\mathrm{salt}]}$, where [salt] is the monovalent ion concentration in mol/L (34). The modified atomic distances entering the GB equation are given by

$$r_{ij}^{\mathrm{GB}} = \sqrt{r_{ij}^2 + \alpha_i \alpha_j \exp\left\{-\frac{r_{ij}^2}{8\alpha_i\alpha_j}\right\}}. \qquad (S34)$$

Critical quantities for the accuracy of the GB model are the Born radii α_i, which essentially express how far each atom is from the molecular surface. To calculate these, we use the GB-MV2 method (35, 36) implemented in the CHARMM software (37), which was shown to yield very good accuracy compared to Poisson-Boltzmann results.

Because all energies in the MM-GBSA framework are expressed in terms involving single atoms or pairs of atoms, ΔG_{bind} can be decomposed in contributions from separate groups of atoms (29, 30). For the Van der Waals, electrostatic, and GB pair terms, half of the interaction energy is attributed to each atom of the pair. When applied to amino acid side chains, this decomposition yields contributions comparable to those obtained by computational alanine scanning (38). In the present case, summing over all residues in M or P allows us to attribute contributions of each binding partner to ΔG_{bind}. These contributions can differ due to different desolvation penalties on each side. The MM-GBSA free energy decomposition were carried out using a custom set of scripts built upon the original implementation of V. Zoete (30, 38, 39) and the CHARMM version 37 software (37).

To perform the MM-GBSA analysis on each of the two MA/membrane systems, we first created a single trajectory file by concatenating the last ~150 ns from the respective replica simulations of a single MA and the bilayer. The trajectories of the –Chol and +Chol systems consisted of a total of 5929 and 3450 frames, respectively, all output with a stride of 80 ps. Only the top membrane leaflet was considered in the reported energy analysis (taking the bottom leaflet into account had an insignificant effect on the energies). The calculation was set up and run with 50 mM salt and a 20 Å cutoff for VdW and electrostatics.

ESR measurements. ESR was performed as previously described (40) with the following changes. Multilamellar vesicles were extruded to form 100 nm large unilamellar vesicles (LUVs). The LUVs were incubated with MA protein at a ratio of 0.31 mg protein to 1 mg lipid (the same ratio used for SANS measurements) in buffer (20 mM Tris HCl pH 8, 50 mM NaCl, 2 mM TCEP) for no less than 30 minutes at ambient room temperature (~22 °C) prior to loading into glass ESR capillary tubes. The final protein concentration in the ESR experiment was ~ 68 μM, or approximately three times the MA binding constant measured by SPR (41) for similar binding reactions. The model-free order parameters for POPC/POPS LUVs with and without MA were each 0.11, and the model-free order parameters for POPC/POPS/Chol LUVs with and without MA were each 0.22 (42).

Continuum mean-field modeling of MA protein-membrane interactions. To quantify the extent of lipid segregation around the MA protein adsorbed to a membrane, we used a previously developed continuum mean-field (CMF) computational approach (43, 44). The CMF method quantifies essential components of the energetics of protein-lipid interactions and describes the combined kinetic effect of many lipid species interacting with the membrane-adsorbed protein. The protocol defines the steady state of the system consisting of the membrane-associated protein, and includes all important degrees of freedom (electrostatics, mixing entropy of lipids and solution ions), as described in detail in our publications (43-47). To this end, a hybrid representation of the computational model is constructed in which membrane-associated proteins are treated at detailed atomic level in three dimensions, and the lipid membrane is considered as a continuum

elastic medium comprised of two-dimensional smooth charged surfaces representing the lipid polar headgroups, and a low-dielectric hydrocarbon core volume.

This system is subjected to a self-consistent minimization of the governing mean-field-based free energy functional F that depends on local lipid component densities $\varphi(x,y)$ and mobile ion concentrations c_+ and c_- (for positive and negative ionic species, respectively) in the solution. In particular, as detailed in (43, 44), F can be written as the sum of electrostatic energy (F_{el}), lipid mixing entropy (F_{lip}), and salt ion translational entropy (F_{ion}) contributions:

$$F = F_{el} + F_{lip} + F_{ion}, \quad (S35)$$

where,

$$F_{el} = \frac{1}{2}\epsilon_0\epsilon_w\left(\frac{k_BT}{e^2}\right)\int_V (\nabla\Phi)^2 dv, \quad (S36)$$

$$F_{lip} = \frac{k_BT}{a}\int_A \left[\varphi\, ln\frac{\varphi}{\varphi_0} + (1-\varphi)\, ln\frac{(1-\varphi)}{(1-\varphi_0)}\right] dA, \quad (S37)$$

$$F_{ion} = k_BT\int_V \left[c_+\, ln\frac{c_+}{c_0} + c_-\, ln\frac{c_-}{c_0} - (c_+ + c_- - 2c_0)\right] dv. \quad (S38)$$

In the above, k_B is the Boltzmann constant, T is the temperature, e is the elementary charge, ϵ_0 is the permeability of free space, and $\epsilon_w = 80$ is the dielectric constant of the aqueous solution. Φ represents reduced (dimensionless) electrostatic potential in space, a denotes the area per lipid, c_0 is the salt concentration in the bulk, and φ_0 represents bulk concentration of a charged lipid species. The $\varphi(x,y)$ local field relates to the surface charge densities $\sigma(x,y)$ through $\sigma(x,y) = (e/a)\varphi(x,y)z(x,y)$, where $z(x,y)$ denotes valency of the lipid at (x,y). Minimization of F with respect to c_+ and c_- leads to the non-linear Poisson-Boltzmann (NLPB) equation (48):

$$\nabla\Phi = \lambda^{-2}\, sinh\,\Phi, \quad (S39)$$

which is solved to obtain Φ in space (λ being the Debye length of the electrolyte solution). As seen from Eqs. S35-38, this electrostatic potential is self-consistently dependent on the local lipid concentrations through the entropic penalty (F_{lip}) due to lipid segregation or de-mixing. Thus, a self-consistent search for the free energy minimum is conveniently carried by linking Φ (obtained from the NLPB equation) and spatial charged-lipid compositions φ on each leaflet of the membrane to the respective electrochemical potentials μ through the Cahn-Hilliard (CH) equation (49):

$$\frac{\partial \varphi(\vec{r},t)}{\partial t} = D_{lip}\nabla^2\mu(\vec{r},t). \qquad (S40)$$

To quantify interactions between MA protein and the membrane composed of 70/30 mol% mixture of POPC/POPS lipids with the CMF approach, we took one of the top 5 simulation frames with the lowest MA-bilayer total interaction energy (as calculated from MM/GBSA). Then, by applying only global transformations to the protein, we positioned MA in a manner where we maximized the exposure of its lysine residues to a flat lipid surface of $\sigma(x,y) \sim 4.93\times10^{-3}$ e^- charge density, corresponding to ~30 mol% PS lipid content (assuming a = 60.9 $Å^2$).

The self-consistent minimization of F was then carried out for the protein by solving the NLPB equation using the multigrid solver of the Adaptive Poisson-Boltzmann Solver (APBS) suite (50) on 1 Å-spaced cubic 256 $Å^3$ mesh as described previously (43). This was done using a 0.05 M ionic solution of monovalent counterions (corresponding to λ = 13.49 Å Debye length), and a dielectric constant of 2 for the membrane interior and protein, and 80 for the solution. The protein models were positioned so that the minimum distance between the protein and the lipid surface was 2 Å (43, 47).

The CMF calculation shows the adsorption free energy of MA protein, $\Delta F = F-(F_{prot}+F_{memb})$ (F_{prot} and F_{memb} representing the free energy of protein and membrane system in separation) onto the POPC/POPS 70/30 mol% lipid membrane is ~ –9 k_BT (see Fig. S4A). Importantly, lipid de-mixing had an insignificant effect on ΔF (the minimization procedure resulted in a change in ΔF of < 1 k_BT, Fig. S4A) as the local concentration of PS under the adsorbed protein calculated by integrating the charge map of the smallest rectangle enclosing the protein shadow, was ~ 31%, or only slightly higher than the bulk PS concentration of 30% (see Fig. S4B). The minor extent of lipid segregation, together with the concomitant insignificant change in the adsorption free energy, suggests that MA protein adsorbs onto the PC/PS membrane mainly through the electrostatic sensing of PS lipid domains.

SUPPORTING TABLES

Table S1. Protein crystallization conditions, and statistics associated with the X-ray diffraction data and atomic models.

Protein	**RSV MA**	**RSV MA_{2-102}**	**RSV MA_{2-102}**
Crystallization Conditions			
Protein concentration (μM)	680	540	540
Reservoir Solution	2.60 M Ammonium formate 0.20 M β-Alanine/KOH pH 10.3	18%(w/v) PEG 8000 0.2 M Succinic acid/KOH pH 5.5 1.0 M Ammonium nitrate	0.6 M Malonic acid /KOH pH 9.1 0.1 M Boric acid /KOH pH 9.1
Temperature (°C)	Ambient	18	18
X-ray diffraction data			
Cryoprotectant	4.00 M Ammonium formate 0.20 M β-Alanine/KOH pH 10.3 30 %(v/v) Ethylene glycol	20%(w/v) PEG 8000 0.1 M Succinic acid/KOH pH 5.5 1.0 M Ammonium nitrate 20 %(v/v) Ethylene glycol	0.6 M Malonic acid /KOH pH 9.1 0.1 M Boric acid /KOH pH 9.1 20 %(v/v) Ethylene glycol
Space group	$I4_122$	$I4_1$	$I4_122$
Unit cell lengths (Å)	a=b= 66.2, c= 218.8	a=b= 79.0, c= 27.8	a=b= 67.4, c=220.8
X-ray source	ALS Beamline 8.2.1	Rigaku MicroMax-007 HF Rotating Copper Anode	Rigaku MicroMax-007 HF Rotating Copper Anode
X-ray wavelength (Å)	1.03320	1.54179	1.54179
Sample Temperature (K)	100	110	110
Data resolution limits (Å) [a]	49.0 - 2.85 (2.95 - 2.85)	39.5 - 1.86 (1.93 - 1.86)	49.7 - 3.20 (3.31 - 3.20)
Number of unique observations [a]	6104 (582)	7363 (681)	4535 (429)
Mean Redundancy [a]	8.7 (9.0)	12.4 (11.4)	10.1 (10.5)
Completeness (%) [a]	99.9 (100.0)	99.5 (94.6)	99.9 (100.0)
$R_{measure}$ [a]	ND (ND)	0.058 (0.289)	0.139 (0.703)
R_{merge} [a]	0.070 (0.455)	0.055 (0.277)	0.132 (0.678)
Mean I / σI [a]	34.0 (4.1)	56.0 (10.0)	22.2 (4.5)
Crystallographic models			
Number of protein molecules in the asymmetric unit	1	1	1
R_{work} / R_{free} [b]	0.195 / 0.239	0.164 / 0.210	0.202 / 0.249
Total number of protein atoms	767	741	791
Number of water molecules	7	54	6
Other ligands	-	Ethylene Glycol NO_3^-	-
Disorder Model	Individual Isotropic B-factors	Individual Isotropic B-factors	Individual Isotropic B-factors
Mean total isotropic B-factor, all protein atoms ($Å^2$):	67.4	23.1	74.7
Bulk Solvent model	Mask	Mask	Mask
RMSD from ideal geometry : Bond lengths (Å) / Bond angles (°)	0.008 / 1.325	0.011 / 1.392	0.013 / 1.695
Residues in Favoured / Allowed regions of Ramachandran plot (%)[c]	100.0 / 100.0	97.1 / 100.0	95.3 / 100.0
PDB ID code	5KZ9	5KZA	5KZB

[a]Numbers in parentheses are for the highest resolution shell. [b]Calculated from a randomly selected 5% of observations omitted from all model refinement. [c]Defined by the MolProbity web-server (51).

Table S2. Bilayer structural parameters obtained from the refinement of SANS data. Italicized values indicate constrained parameters, and asterisks indicate parameters that were varied during the fitting routine (all remaining structural and compositional values are obtained through mathematical relationships).

Parameter	– Cholesterol		+ Cholesterol	
	– RSV-MA	+ RSV-MA	– RSV-MA	+ RSV-MA
global				
χ_{POPC}	*0.7*	*0.7*	*0.34*	*0.34*
χ_{POPS}	*0.3*	*0.3*	*0.3*	*0.3*
χ_{CHOL}	--	--	*0.36*	*0.36*
POPC-rich domain				
χ_{POPC}	0.9 ± 0.1*	0.9 ± 0.1*	0.46 ± 0.02*	0.45 ± 0.07*
χ_{POPS}	0.1 ± 0.1	0.1 ± 0.1	0.18 ± 0.02	0.19 ± 0.07
χ_{CHOL}	--	--	*0.36*	*0.36*
V_L [Å^3] [a]	1234 ± 2	1236 ± 2	1012 ± 1	1012 ± 2
A_L [Å^2] [b]	63.1 ± 1.4*	61.5 ± 2.0*	48.2 ± 0.6*	47.7 ± 0.9*
D_B [Å] [c]	39.2 ± 0.9	40.3 ± 1.2	42.0 ± 0.5	42.4 ± 0.8
$2D_C$ [Å] [d]	29.0 ± 0.7	29.9 ± 0.9	33.8 ± 0.4	34.1 ± 0.6
D_H [Å] [e]	6.9 ± 1.5*	6.2 ± 0.6*	7.2 ± 1.4*	6.6 ± 1.3*
POPS-rich domain				
χ_{POPC}	0.3 ± 0.3	0.3 ± 0.3	0.08 ± 0.03	0.19 ± 0.09
χ_{POPS}	0.7 ± 0.3	0.7 ± 0.3	0.56 ± 0.03	0.45 ± 0.09
χ_{CHOL}	--	--	*0.36*	*0.36*
V_L [Å^3] [a]	1222 ± 5	1222 ± 5	1003 ± 2	1005 ± 3
A_L [Å^2] [b]	63.0 ± 4.3*	65.2 ± 2.3*	48.8 ± 4.4*	47.4 ± 2.9*
D_B [Å] [c]	38.9 ± 1.4	38.6 ± 0.9	41.7 ± 1.9	42.2 ± 1.3
$2D_C$ [Å] [d]	29.1 ± 1.1	29.0 ± 0.6	33.8 ± 1.5	34.2 ± 1.0
D_H [Å] [e]	9.2 ± 1.0*	6.4 ± 1.3*	7.8 ± 1.7*	7.6 ± 1.8*
Protein bound to POPS-rich domain				
A_P [Å^2] [f]		*1375*		*1375*
z_P [Å] [g]	--	35.9 ± 0.8*	--	38.0 ± 0.6*
σ_P [Å] [h]	--	7.2 ± 0.6*	--	6.6 ± 0.4*
N_L [i]	--	21 ± 1	--	29 ± 2
N_{POPS} [j]	--	15 ± 5	--	13 ± 3
f_P [k]	--	0.47 ± 0.04*	--	0.50 ± 0.05*
a_P [l]	--	0.35 ± 0.04	--	0.40 ± 0.04

[a]average lipid volume calculated as mole fraction-weighted sum of lipid and chol molecular volumes [b]average area per lipid [c]total bilayer (Luzzati) thickness [d]bilayer hydrocarbon thickness [e]headgroup thickness [f]area per protein [g]center of Gaussian protein volume distribution [h]width of Gaussian protein volume distribution [i]average number of outer leaflet lipids in protein shadow [j]average number of outer leaflet POPS in protein shadow [k]fraction of protein bound to vesicle [l]vesicle area fraction bound by protein

Table S3. Molecular volume V, neutron scattering length b, and neutron scattering length density ρ of different species.

	V [Å^3]		b [fm]		ρ [fm Å^{-3}]	
D_2O	30.1		19.145		0.636	
RSV-MA in D_2O	20280[a]		6325[b]		0.312	
	Head	*Chains*	*Head*	*Chains*	*Head*	*Chains*
POPC[c]	331	916	60.072	-26.624	0.181	-0.029
POPC-D31[c]	331	916	60.072	296.086	0.181	0.323
POPS[d]	278	917	115.789	-26.624	0.417	-0.029
POPS-D31[d]	278	917	115.789	296.086	0.417	0.323

[a]sum of residue volumes taken from ref. (52) [b]accounts for exchangeable protons following ref. (53) [c]volume data from ref. (54) [d]volume data from ref. (55)

Table S4. Estimated composition (56-58) and surface charge density (calculated from the mole fraction-weighted charge and area) of the mammalian plasma membrane inner leaflet.

lipid	mole fraction χ	charge [e$^-$]		area [Å^2]	
		per lipid	χ-weighted	per lipid	χ-weighted
Chol	0.4	0	0	27[a]	10.8
(PO)PE	0.28	0	0	59[b]	16.5
(PO)PC	0.05	0	0	65[c]	3.3
(PO)PS	0.18	-1	0.18	64[d]	11.5
(SA)PI	0.08	-1	0.08	68[e]	5.4
(SA)PIP2	0.02	-3	0.06	68[e]	1.4
Total	1.0		0.32		48.9

[a]ref. (59) [b]ref. (60) [c]ref. (54) [a]ref. (55) [e]ref. (61)

Table S5. Decomposition of the interaction energy of MA and the lipids calculated with the MM-GBSA method from the simulation trajectories as described in the SM text. Shown are the Van der Waals (VdW) and electrostatic (Elec) energies calculated in vacuum and their sum, $\Delta E_{\mathrm{int}}^{\mathrm{vac}}$; the polar (P) and nonpolar (NP) desolvation penalties and their sum, $\Delta\Delta G_{solv}$; and the total binding free energy approximated by $\Delta E_{\mathrm{int}}^{\mathrm{vac}}+\Delta\Delta G_{solv}$. All energy units are in kcal/mol.

system	component	Interaction energy in vacuum			Desolvation penalty			total
		VdW	Elec	ΔG_{in}^{vac}	P	NP	$\Delta\Delta G_{solv}$	
MA and PC/PS	MA	-9.3	-607.8	-617.1	620.9	-4.8	616.1	-1.0
	lipids	-9.3	-607.8	-617.1	620.6	-4.2	616.4	-0.7
MA and PC/PS/Chol	MA	-8.5	-765.6	-774.1	779.1	-5.1	774.0	-0.1
	lipids	-8.5	-765.7	-774.1	773.1	-4.8	768.3	-5.8

SUPPORTING FIGURES

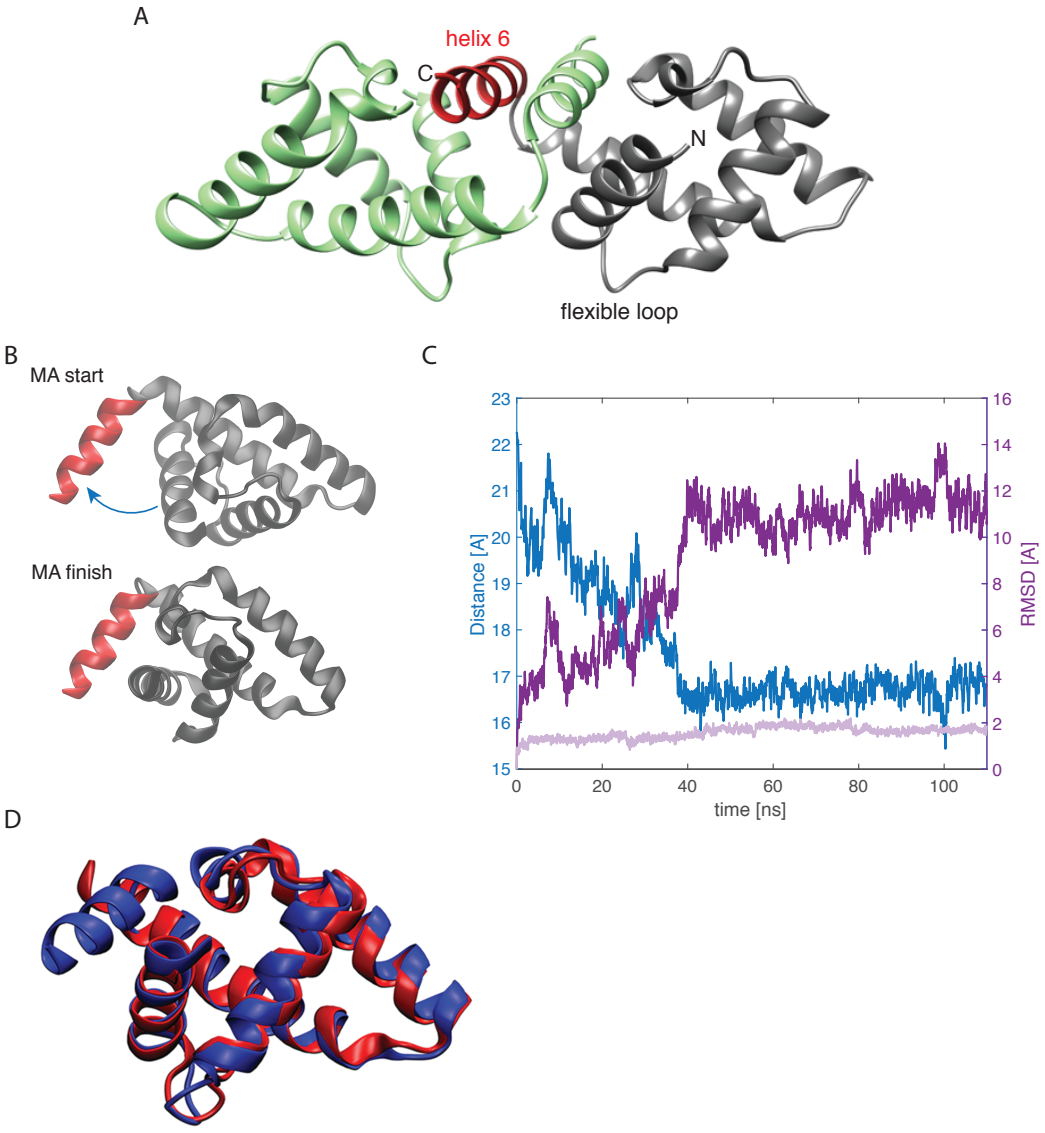

Figure S1. (A) Crystal structure of the resolved MA dimer, with monomers colored in green and grey. Helix 6 of the grey-colored monomer is shown in red. (B) Snapshots of the protein at the start and finish of the water box simulation. Helix 6 (red) is fixed during the simulation and is displayed in the same plane while the rest of the protein (referred to protein *body* from here on) rotates ~ 30 degrees. An arrow denotes the observed structural change. (C) Time evolution of the distance between the centers of mass of helix 6 and the protein body (residues 1-90, blue). Also plotted are the *full protein backbone* RMSD with respect to the starting structure after alignment on helix 6 (dark purple) and the *protein body* RMSD after alignment on the protein body (light purple). (D) Overlay of the monomer crystal structure of MA (red) and the structure of MA used in the simulations (blue). The backbone RMSD between the two structures (excluding helix 6 which is not present in the monomer crystal structure) is 2.8 Å.

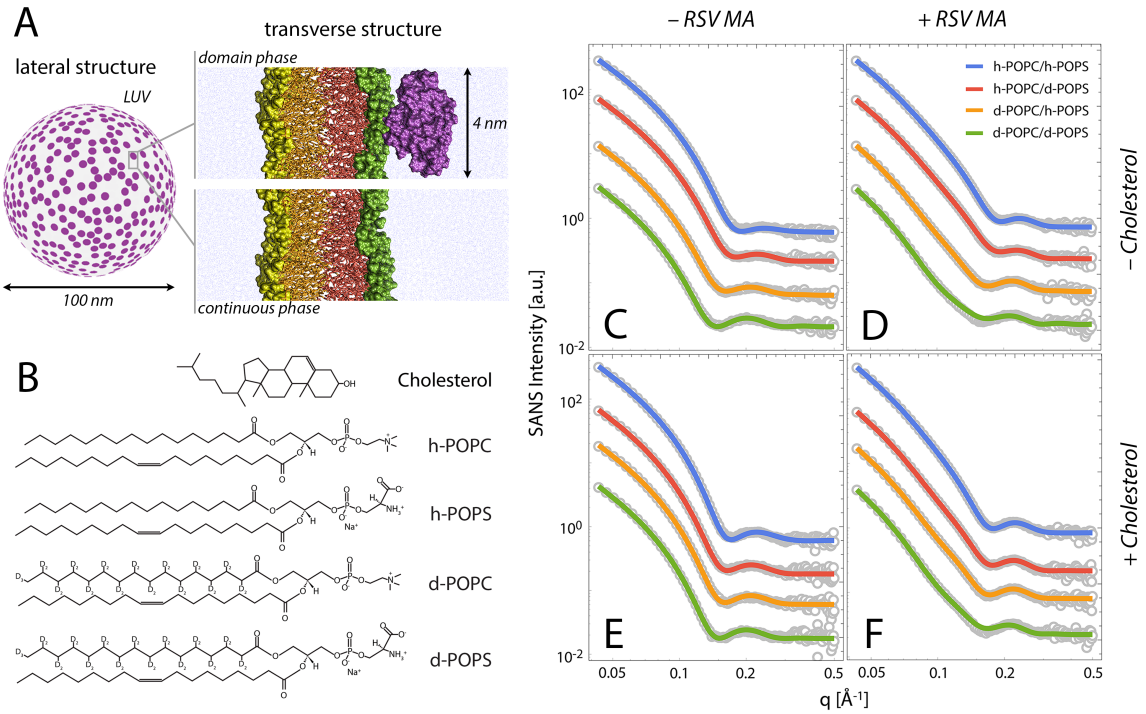

Figure S2. Bilayer structure from analysis of SANS data. (A) Schematic illustration of a 100 nm LUV and the two environments used in the model to analyze the SANS data. The structural model accounts for both transverse and lateral structure. Transverse structure arises from the layered distribution of matter projected onto the bilayer normal, and is mathematically described by parameters related to the volume probability distributions of inner and outer leaflet lipid headgroups, and hydrocarbon chains, in addition to bound protein. Lateral structure can arise from lipid clustering or phase separation, as well as partial surface coverage of bound protein monomers; it is mathematically described by parameters related to the domain size, shape and spatial arrangement (here, domains were modeled as circular disks, randomly arranged on the vesicle surface). Two distinct coexisting environments were modeled—the domain and the surrounding continuous phase—with the lipid composition and transverse structure of each allowed to vary as described in the SM text. (B) Structures of lipids used in SANS experiments. Palmitoyl chain-perdeuterated variants of POPC and POPS (i.e., d-POPC and d-POPS) were used to provide a scattering length density contrast in order to highlight lateral structure. (C-F) Scattering data (open circles) and fits (solid lines) for four different neutron contrast data sets, with different sample compositions: POPC/POPS 70/30 mol% (C); POPC/POPS 70/30 mol% + RSV MA (D); POPC/POPS/Chol 34/30/36 mol% (E); POPC/POPS/Chol 34/30/36 mol% + RSV MA (F).

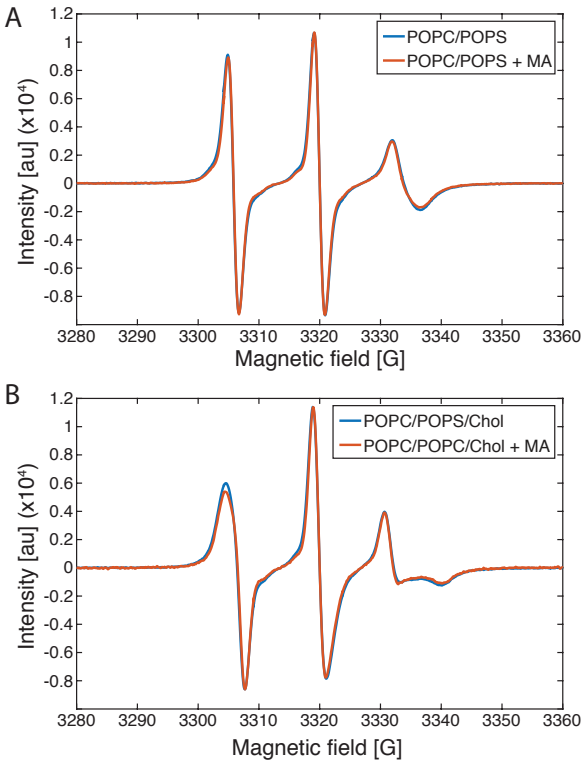

Figure S3. ESR spectra of (A) POPC/POPS with and without MA, and (B) POPC/POPS/Chol with and without MA. All LUVs contained 0.5 mol% of 16:0-16 Doxyl PC.

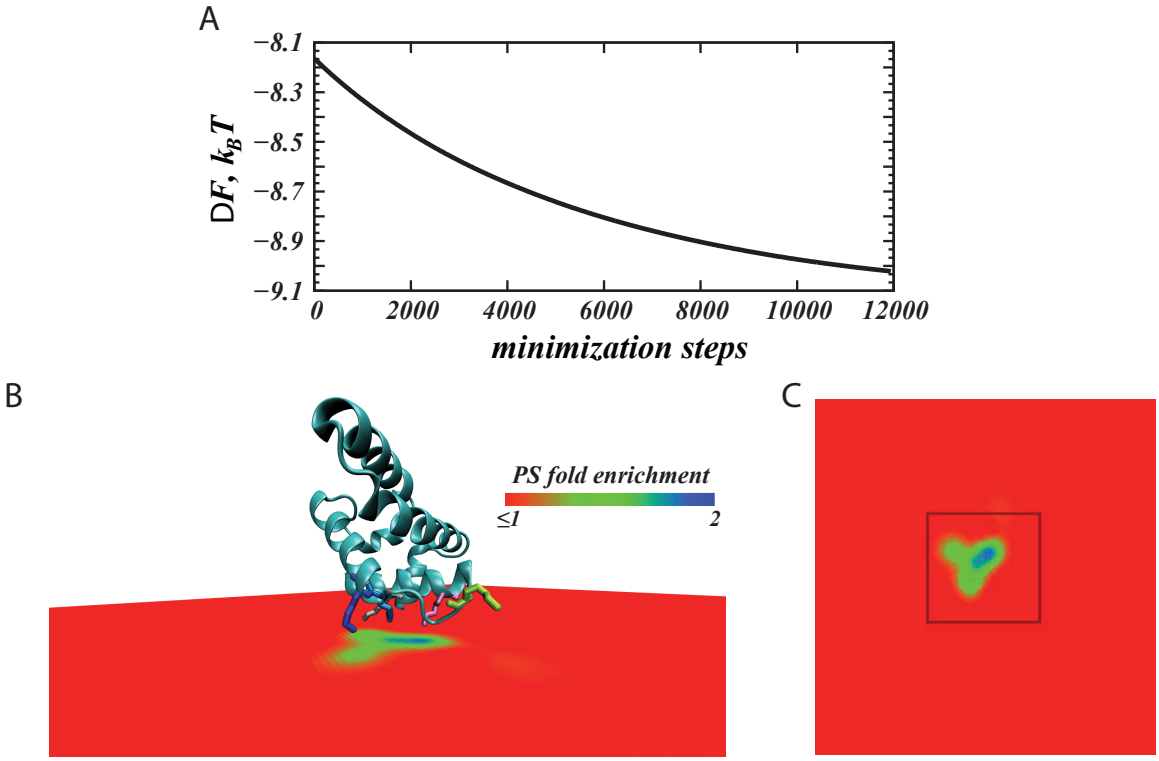

Figure S4: (A) Convergence of the adsorption free energy (ΔF) in the CMF calculations. Shown is the change in ΔF as the mean-field free energy functional is minimized. Value of ΔF at 0^{th} minimization step corresponds to the adsorption free energy onto homogeneous membrane composed of charged and neutral lipids generating a surface charge density of 4.93×10^{-3} e^- (corresponding to a PC/PS lipid mixture with ~30 mol% PS). (B) View of the MA protein (cartoon) adsorbing on the lipid membrane (as seen from the side). The level of PS lipid segregation by the protein, calculated with CMF approach, is illustrated (as ratios of local and bulk lipid fraction values) in color code. Lysine residues close to the surface are shown in licorice and color according to the following: K6 – gray, K13 – purple, K18 – green, K23 – light blue, K24 – dark blue. (C) View of the lipid membrane (as seen from above). Highlighted with a black box is the smallest rectangle enclosing the protein shadow , whose charge density was integrated to calculate the local concentration of PS under MA (~31 mol%).

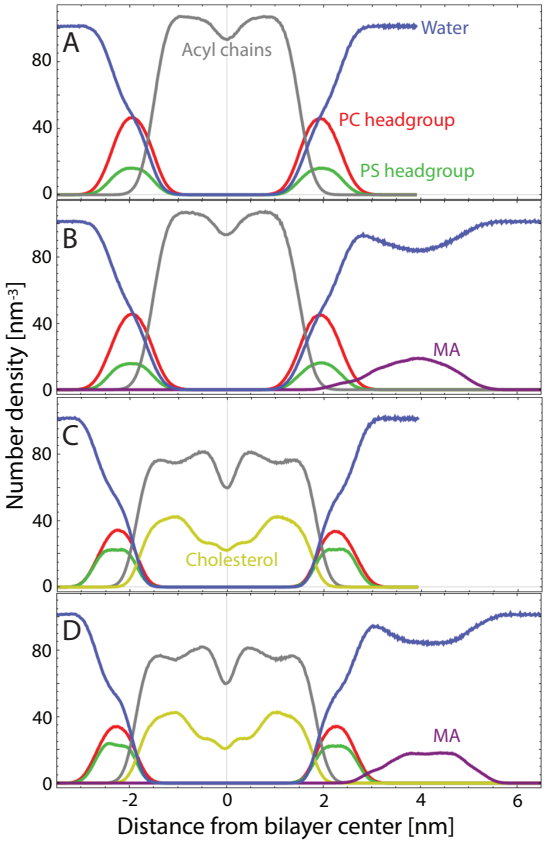

Figure S5. Number density profiles calculated from four different MD simulations. Color coded are the profiles of lipid acyl chains (grey), water (blue), POPC headgroups (red), POPS headgroups (green), Chol (yellow) and MA (purple) calculated from the last 100 ns of each simulation: (A) POPC/POPS 70/30 mol%; (B) POPC/POPS 70/30 mol% with MA; (C) POPC/POPS/Chol 34/30/36 mol%; and (D) POPC/POPS/Chol 34/30/36 mol% with MA.

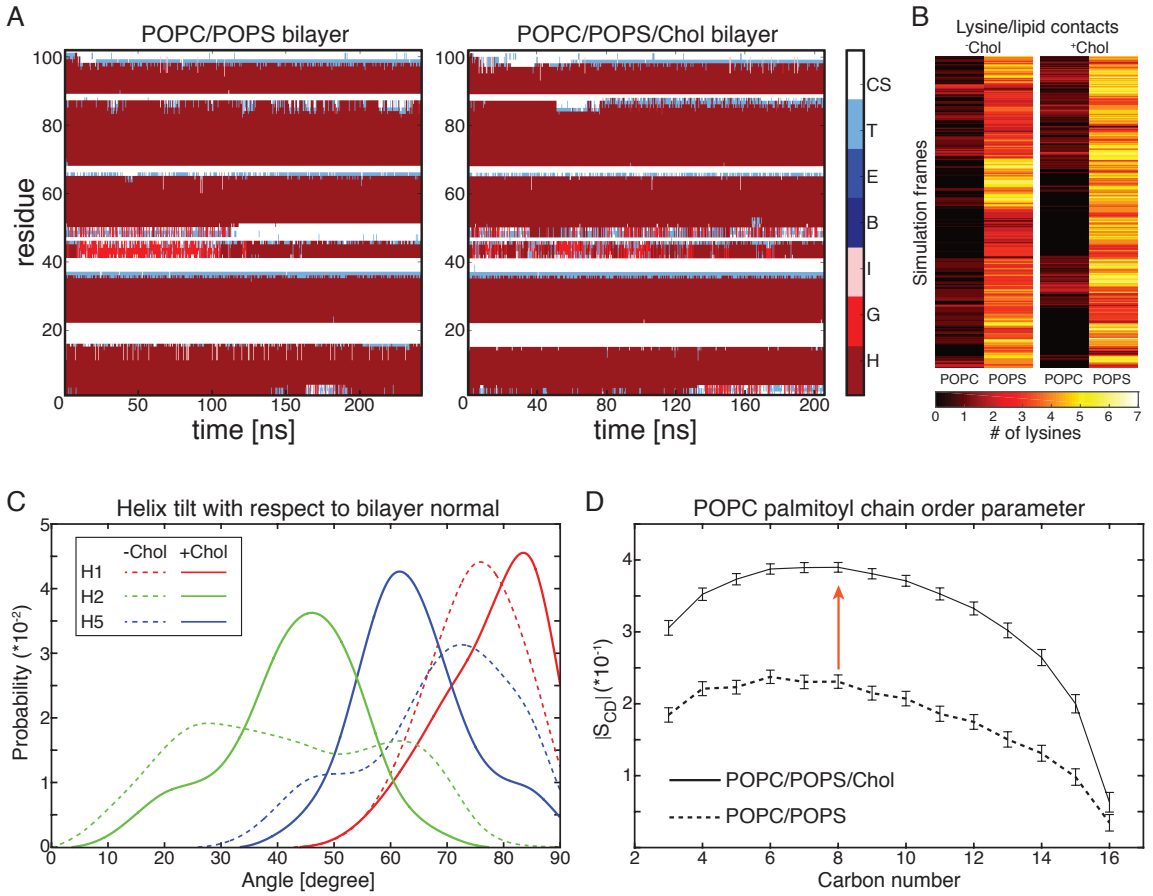

Figure S6. (A) Time evolution of MA's secondary structure in bilayers composed of POPC/POPS 70/30 mol% (left) or POPC/POPS/Chol 34/30/36 mol% (right). The secondary structure assignment of each residue was calculated with the DSSP software. They are as follows: H, alpha helix; G, 3-turn helix; I, pi helix; B, residue in isolated beta-bridge; E, extended beta sheet; T, hydrogen bonded turn; and CS, coil and bend. (B) Heat map of lysine-lipid contacts defined as having no more than 4 Å distance between the centers of mass of the NH_3 Lysine group and either the serine or phosphate groups on the lipid headgroups. Each row represents a single frame and the color denotes the number of instantaneous lysine-POPC or lysine-POPS contacts. Shown is data from the last 100 ns of three replica simulations for each system. (C) Tilt distributions of helices 1, 2 and 5 with respect to bilayer normal. The helices direction vectors are defined by the Cα atoms of residues E2 and K13, K23 and Q34, and E70 and A84, respectively, and the bilayer normal is the z-dimension of the simulation cell. The broad distributions in the absence of Chol indicate the dynamic nature of MA orientation with respect to the membrane (dashed lines, Movie S1A), which becomes more stable upon the addition of Chol (solid lines, Movie S1B). (D) The acyl chain order parameter of the palmitoyl chain of POPC, S_{CD}, increases by more than 65% in the presence of Chol as denoted by the red arrow.

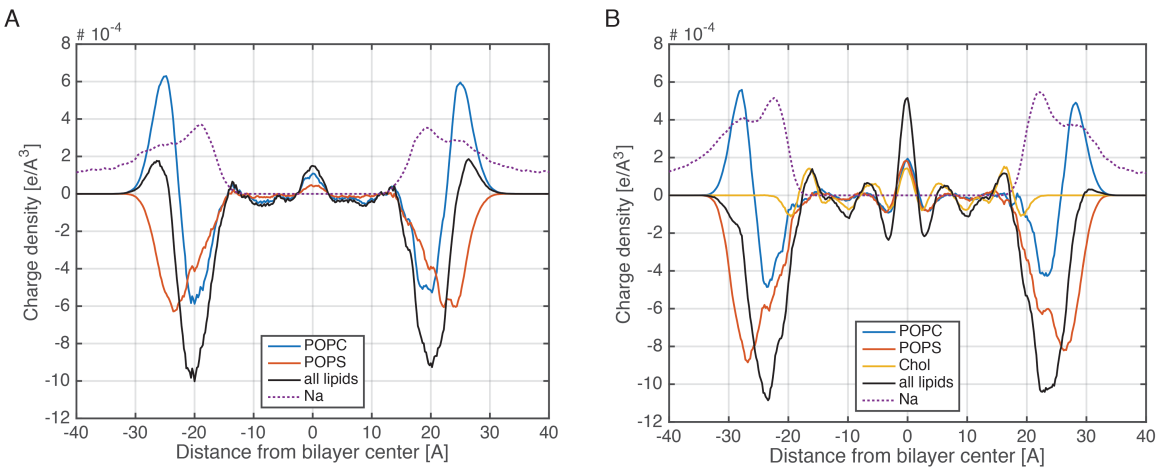

Figure S7. Charge density of POPC (blue), POPS (red), Chol (yellow), all lipids (black) and sodium (dashed purple line) from the two bilayer-only simulations of POPC/POPS (A) and POPC/POPS/Chol (B). The positively charged choline group on the POPC headgroups counteracts the negatively charged serine group on the POPS headgroups, and depending on the PC/PS ratio, the net effect is the accumulation of a higher (A) or lower (B) positive charge density on the bilayer surface (~ 27 and 30 Å, respectively). Note that since the charge density calculation is performed at high resolution (slabs in z with thickness of 0.2 Å) on individual atoms with assigned partial charges, relative imbalances in the distributions of hydrogen and carbon atoms result in a peak of positive charge density at the interface between the two leaflets. If the calculation is instead performed on the neutral chemical atomic groups (e.g. methylene, methyl), instead of the individual atoms, the positive density at the midplane would disappear.

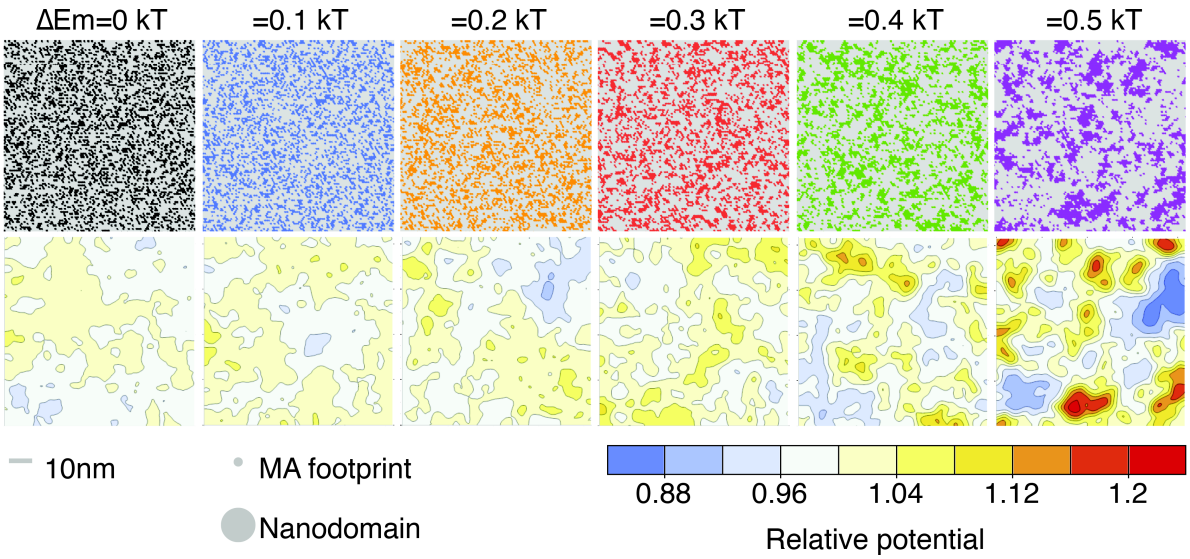

Figure S8. Non-ideal mixing does not induce large changes in membrane surface potential but may influence the spatial organization of bound protein. *Upper*, plots of the lateral distribution of a binary lipid mixture (70/30 mol% neutral/charged) obtained from Monte Carlo lattice simulations. Increasing the unfavorable pairwise interaction energy ΔEm results in larger clusters of the charged lipid (colored regions) within the neutral lipid matrix (gray regions). *Lower*, corresponding maps of the relative electrostatic surface potential calculated 3 Å above the bilayer surface and normalized to the potential of a uniformly mixed bilayer having the same average charge density. Also displayed for reference are the relative sizes of the MA protein (4 nm diameter) and a lipid nanodomain (15 nm diameter (62)). Scale bar 10 nm.

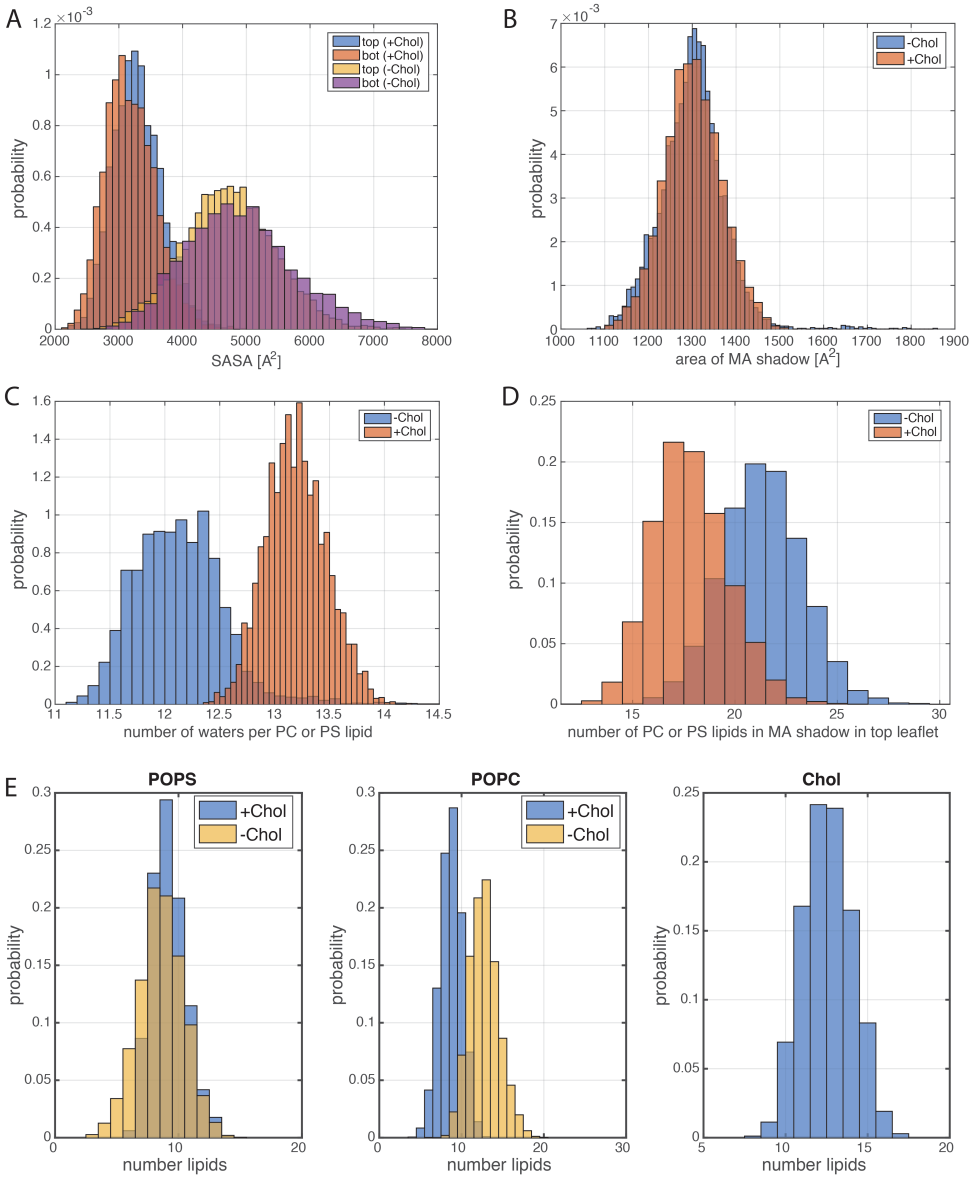

Figure S9. (A) Solvent exposed surface area (SASA) of each leaflet of the bilayer patch in the MA shadow. The MA shadow is defined as the set of atoms whose x and y coordinates are within 3 Å of the x and y coordinates of any protein atom. MA is interacting directly with the top leaflet. (B) Area of the MA shadow calculated as the area of the convex hull containing all 2D atomic coordinates in the MA shadow. (C) Distribution of the number of water molecules per POPC or POPS headgroup calculated from the bilayer-only simulations. A water per headgroup is defined as a water molecule within 3 Å of any lipid atom of a POPC or POPS lipid. (D) Distribution of the number of POPC or POPS lipids in the top leaflet from the MA-bilayer trajectories, whose phosphate atoms are within the MA shadow. (E) Number of different lipid counts in the top leaflet of the bilayer patch in the MA shadow in the two systems. POPS and POPC are represented with their phosphate atoms and Chol with its O3 atom. All distributions in this figure were constructed from calculations performed across all frames of the respective simulation trajectories.

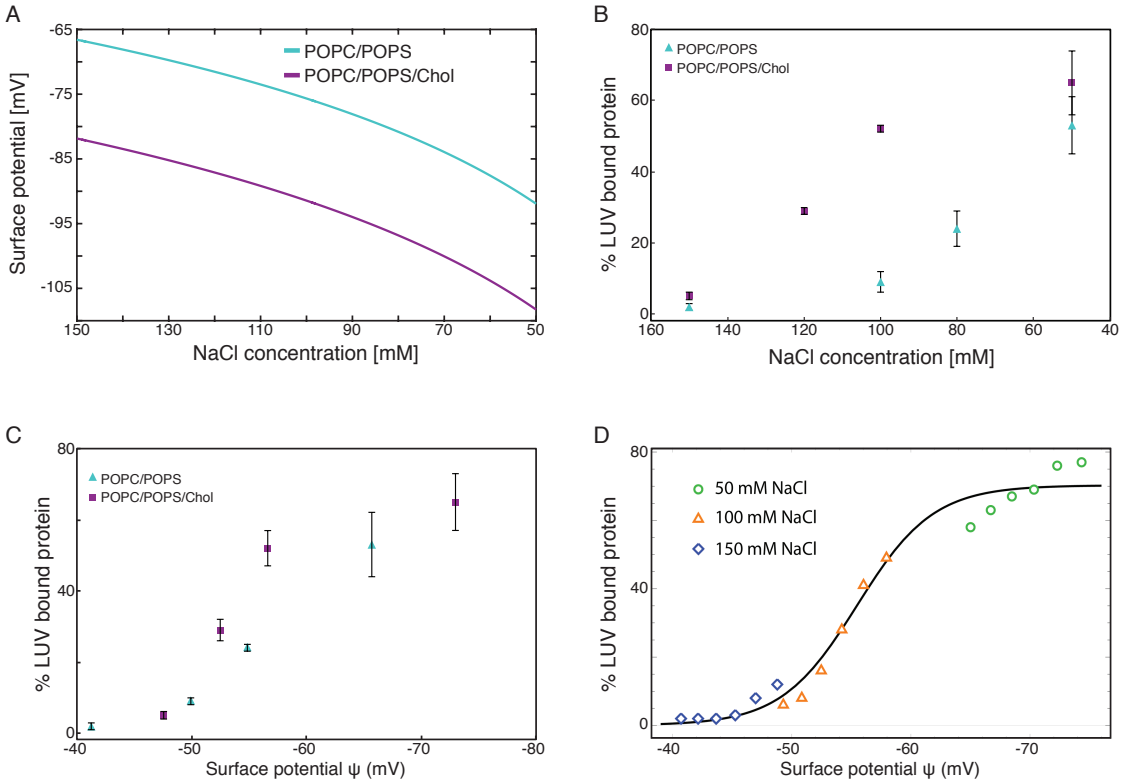

Figure S10. RSV MA membrane association as a function of NaCl concentration. (A) Example of a calculated membrane surface potential as a function of increasing NaCl concentrations for POPC/POPS (70/30 mol%) (light blue) and POPC/POPS/Chol (34/30/36 mol%) (purple) bilayers. (B) % of LUV-bound MA plotted against decreasing NaCl concentration. (C) Binding data from B plotted against calculated membrane surface potential. (D) Best sigmoidal fit to the MA binding data versus surface potential from Fig. 5F (see SM text for more details).

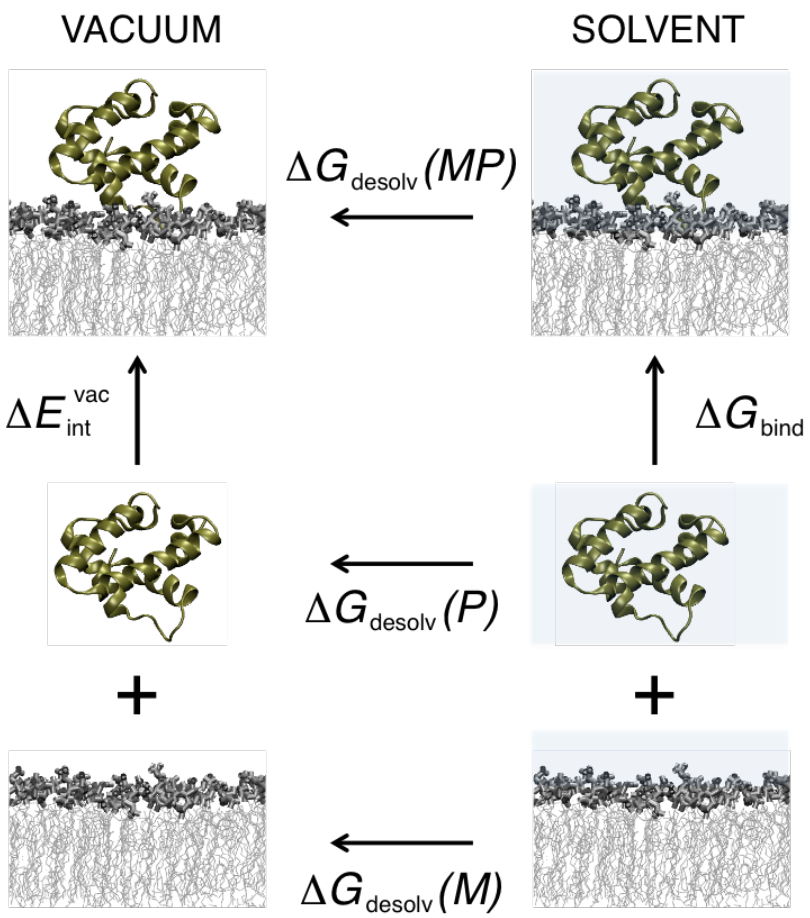

Figure S11: Thermodynamic cycle underlying the MM-GBSA method. For each frame of the trajectory, the binding free energy ΔG_{bind} is estimated from the vacuum interaction energy and the desolvation penalties for each binding partner and the complex.

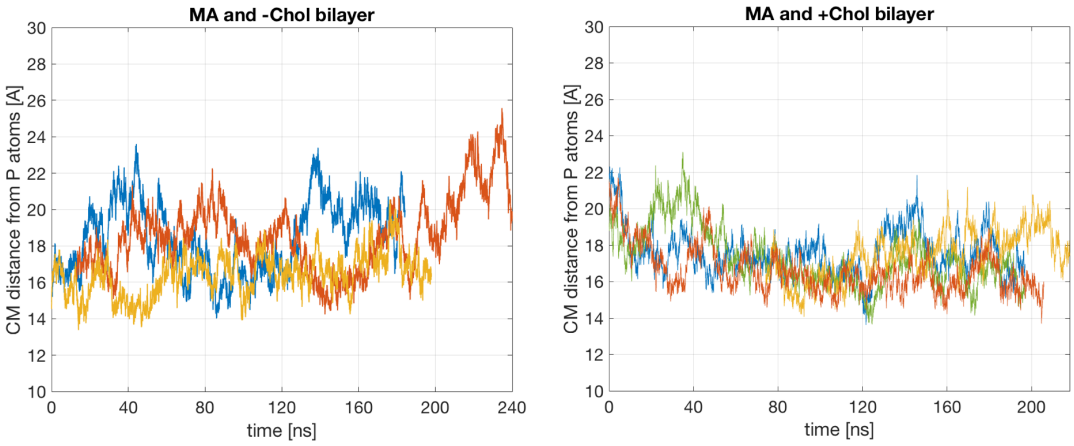

Figure S12. Fluctuations of the distance between MA and bilayer surface. Time evolution of the MA-bilayer distance defined as the distance in z between the center of mass of the protein and the center of mass of the phosphate atoms in the MA-proximal leaflet. Data is shown for the –Chol (left) and +Chol (right) systems. Colors denote different replica simulations (or in the latter also proteins interacting with different leaflets).

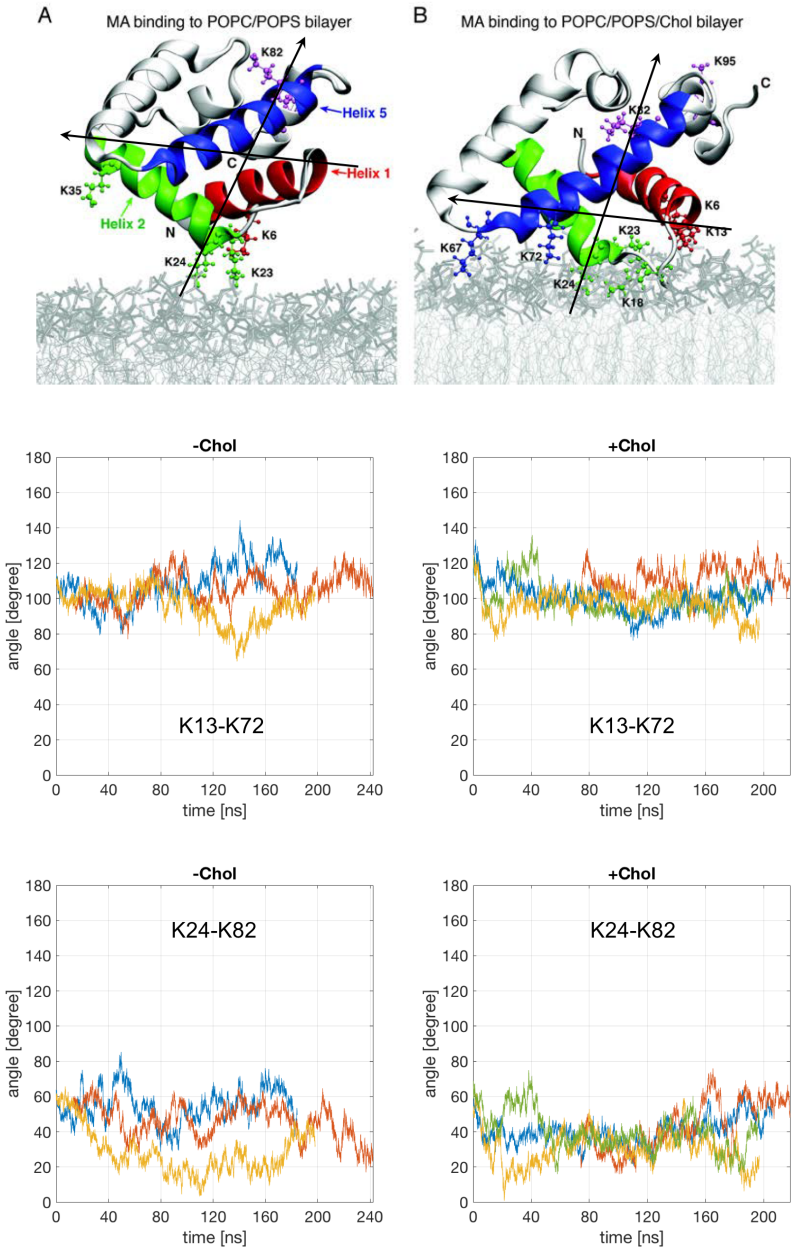

Figure S13. Orientation of MA with respect to the bilayer surface. *Top* Fig. 2AB with two axes (director vectors) shown, defining the orientation of MA relative to the bilayer surface: one, connecting the Cα atoms of K13 and K72, and another one connecting the Cα atoms of K24 and K82. Time evolution of the tilt angle of each axis (middle and bottom rows) with respect to the bilayer normal (z dimension of the simulation box) is shown for the –Chol (left) and +Chol (right) systems. Colors denote different replica simulations (or in the latter also proteins interacting with different leaflets). After about 80 ns of initial relaxation, the tilts fluctuate ~103º for K13-K72 and ~41º for K24-K82 with standard deviations within 10 degrees for individual replicas, and within 16 or 10 degrees across different replicas for –Chol and +Chol systems respectively.

Supporting Movies

SI Movie 1. Cholesterol enhances MA-membrane contacts. Simulation segment showing 40 ns of MA interaction with POPC/POPS .7/.3 (A) and POPC/POPS/Chol .34/.3/.36) (B) membranes. Lipid acyl chains and head groups are in light and dark gray, respectively. MA coloring is as described in main text. All lysine residues are shown in ball-and-stick representation and colored according to the helix to which they belong, except for K18 (gold) which is positioned in a loop, and K95 (silver) which is positioned in helix 6. Water and ion atoms are omitted for viewing clarity.

REFERENCES

1. Heberle, F. A., V. N. P. Anghel, and J. Katsaras. 2015. Scattering from phase-separated vesicles. I. An analytical form factor for multiple static domains. J Appl Crystallogr 48:1391-1404.
2. Heberle, F. A., J. Pan, R. F. Standaert, P. Drazba, N. Kucerka, and J. Katsaras. 2012. Model-based approaches for the determination of lipid bilayer structure from small-angle neutron and X-ray scattering data. European biophysics journal : EBJ 41:875-890.
3. Kingston, R. L., H. M. Baker, and E. N. Baker. 1994. Search designs for protein crystallization based on orthogonal arrays. Acta Crystallogr D Biol Crystallogr 50:429-440.
4. Otwinowski, Z., and W. Minor. 1997. Processing of X-ray diffraction data collected in oscillation mode. Method Enzymol 276:307-326.
5. Schneider, T. R., and G. M. Sheldrick. 2002. Substructure solution with SHELXD. Acta Crystallogr D Biol Crystallogr 58:1772-1779.
6. Bricogne, G., C. Vonrhein, C. Flensburg, M. Schiltz, and W. Paciorek. 2003. Generation, representation and flow of phase information in structure determination: recent developments in and around SHARP 2.0. Acta Crystallogr D Biol Crystallogr 59:2023-2030.
7. Emsley, P., B. Lohkamp, W. G. Scott, and K. Cowtan. 2010. Features and development of Coot. Acta Crystallogr D Biol Crystallogr 66:486-501.
8. Murshudov, G. N., P. Skubak, A. A. Lebedev, N. S. Pannu, R. A. Steiner, R. A. Nicholls, M. D. Winn, F. Long, and A. A. Vagin. 2011. REFMAC5 for the refinement of macromolecular crystal structures. Acta Crystallogr D Biol Crystallogr 67:355-367.
9. McCoy, A. J., R. W. Grosse-Kunstleve, P. D. Adams, M. D. Winn, L. C. Storoni, and R. J. Read. 2007. Phaser crystallographic software. J Appl Crystallogr 40:658-674.
10. Phillips, J. C., R. Braun, W. Wang, J. Gumbart, E. Tajkhorshid, E. Villa, C. Chipot, R. D. Skeel, L. Kale, and K. Schulten. 2005. Scalable molecular dynamics with NAMD. J Comput Chem 26:1781-1802.
11. Humphrey, W., A. Dalke, and K. Schulten. 1996. VMD: visual molecular dynamics. J Mol Graph 14:33-38, 27-38.

12. Touw, W. G., C. Baakman, J. Black, T. A. te Beek, E. Krieger, R. P. Joosten, and G. Vriend. 2015. A series of PDB-related databanks for everyday needs. Nucleic Acids Res 43:D364-368.
13. Jo, S., T. Kim, V. G. Iyer, and W. Im. 2008. CHARMM-GUI: a web-based graphical user interface for CHARMM. J Comput Chem 29:1859-1865.
14. Doktorova, M., D. Harries, and G. Khelashvili. 2017. Determination of bending rigidity and tilt modulus of lipid membranes from real-space fluctuation analysis of molecular dynamics simulations. Physical chemistry chemical physics : PCCP.
15. Dalton, A., P. Murray, D. Murray, and V. Vogt. 2005. Biochemical characterization of rous sarcoma virus MA protein interaction with membranes. J Virol 79:6227-6238.
16. Andelman, D. 2006. Introduction to electrostatics in soft and biological matter. Scot Grad Ser:97-122.
17. Huang, J., and G. W. Feigenson. 1993. Monte Carlo simulation of lipid mixtures: finding phase separation. Biophys J 65:1788-1794.
18. Huang, J., J. E. Swanson, A. R. Dibble, A. K. Hinderliter, and G. W. Feigenson. 1993. Nonideal mixing of phosphatidylserine and phosphatidylcholine in the fluid lamellar phase. Biophys J 64:413-425.
19. Jorgensen, K., M. M. Sperotto, O. G. Mouritsen, J. H. Ipsen, and M. J. Zuckermann. 1993. Phase-Equilibria and Local-Structure in Binary Lipid Bilayers. Biochimica Et Biophysica Acta 1152:135-145.
20. Risbo, J., M. M. Sperotto, and O. G. Mouritsen. 1995. Theory of Phase-Equilibria and Critical Mixing Points in Binary Lipid Bilayers. J Chem Phys 103:3643-3656.
21. Sugar, I. P., T. E. Thompson, and R. L. Biltonen. 1999. Monte Carlo simulation of two-component bilayers: DMPC/DSPC mixtures. Biophysical Journal 76:2099-2110.
22. Frazier, M. L., J. R. Wright, A. Pokorny, and P. F. F. Almeida. 2007. Investigation of domain formation in sphingomyelin/cholesterol/POPC mixtures by fluorescence resonance energy transfer and Monte Carlo simulations. Biophysical Journal 92:2422-2433.
23. Honerkamp-Smith, A. R., P. Cicuta, M. D. Collins, S. L. Veatch, M. den Nijs, M. Schick, and S. L. Keller. 2008. Line tensions, correlation lengths, and critical exponents in lipid membranes near critical points. Biophysical Journal 95:236-246.
24. Heberle, F. A., and G. W. Feigenson. 2011. Phase separation in lipid membranes. Cold Spring Harb Perspect Biol 3.
25. Dai, J. A., M. Alwarawrah, M. R. Ali, G. W. Feigenson, and J. Y. Huang. 2011. Simulation of the l(o)-l(d) Phase Boundary in DSPC/DOPC/Cholesterol Ternary Mixtures Using Pairwise Interactions. Journal of Physical Chemistry B 115:1662-1671.
26. Lis, M., L. Pintal, J. Swiatek, and L. Cwiklik. 2012. GPU-Based Massive Parallel Kawasaki Kinetics in the Dynamic Monte Carlo Simulations of Lipid Nanodomains. Journal of Chemical Theory and Computation 8:4758-4765.
27. Meerschaert, R. L., and C. V. Kelly. 2015. Trace membrane additives affect lipid phases with distinct mechanisms: a modified Ising model. Eur Biophys J Biophy 44:227-233.

28. Srinivasan, J., M. W. Trevathan, P. Beroza, and D. A. Case. 1999. Application of a pairwise generalized Born model to proteins and nucleic acids: inclusion of salt effects. Theor Chem Acc 101:426-434.
29. Gohlke, H., C. Kiel, and D. A. Case. 2003. Insights into protein-protein binding by binding free energy calculation and free energy decomposition for the Ras-Raf and Ras-RaIGDS complexes. Journal of Molecular Biology 330:891-913.
30. Zoete, V., M. Meuwly, and M. Karplus. 2005. Study of the insulin dimerization: binding free energy calculations and per-residue free energy decomposition. Proteins 61:79-93.
31. Srinivasan, J., T. E. Cheatham, P. Cieplak, P. A. Kollman, and D. A. Case. 1998. Continuum solvent studies of the stability of DNA, RNA, and phosphoramidate - DNA helices. Journal of the American Chemical Society 120:9401-9409.
32. Best, R. B., X. Zhu, J. Shim, P. E. Lopes, J. Mittal, M. Feig, and A. D. Mackerell, Jr. 2012. Optimization of the additive CHARMM all-atom protein force field targeting improved sampling of the backbone phi, psi and side-chain chi(1) and chi(2) dihedral angles. J Chem Theory Comput 8:3257-3273.
33. Still, W. C., A. Tempczyk, R. C. Hawley, and T. Hendrickson. 1990. Semianalytical Treatment of Solvation for Molecular Mechanics and Dynamics. Journal of the American Chemical Society 112:6127-6129.
34. Onufriev, A., D. Bashford, and D. A. Case. 2004. Exploring protein native states and large-scale conformational changes with a modified generalized born model. Proteins-Structure Function and Bioinformatics 55:383-394.
35. Lee, M. S., M. Feig, F. R. Salsbury, and C. L. Brooks. 2003. New analytic approximation to the standard molecular volume definition and its application to generalized born calculations. Journal of Computational Chemistry 24:1348-1356.
36. Lee, M. S., F. R. Salsbury, and C. L. Brooks. 2002. Novel generalized Born methods. J Chem Phys 116:10606-10614.
37. Brooks, B. R., C. L. Brooks, A. D. Mackerell, L. Nilsson, R. J. Petrella, B. Roux, Y. Won, G. Archontis, C. Bartels, S. Boresch, A. Caflisch, L. Caves, Q. Cui, A. R. Dinner, M. Feig, S. Fischer, J. Gao, M. Hodoscek, W. Im, K. Kuczera, T. Lazaridis, J. Ma, V. Ovchinnikov, E. Paci, R. W. Pastor, C. B. Post, J. Z. Pu, M. Schaefer, B. Tidor, R. M. Venable, H. L. Woodcock, X. Wu, W. Yang, D. M. York, and M. Karplus. 2009. CHARMM: The Biomolecular Simulation Program. Journal of Computational Chemistry 30:1545-1614.
38. Zoete, V., and O. Michielin. 2007. Comparison between computational alanine scanning and per-residue binding free energy decomposition for protein-protein association using MM-GBSA: Application to the TCR-p-MHC complex. Proteins-Structure Function and Bioinformatics 67:1026-1047.
39. Zoete, V., M. B. Irving, and O. Michielin. 2010. MM-GBSA binding free energy decomposition and T cell receptor engineering. J Mol Recognit 23:142-152.
40. Dick, R. A., S. L. Goh, G. W. Feigenson, and V. M. Vogt. 2012. HIV-1 Gag protein can sense the cholesterol and acyl chain environment in model membranes. Proc Natl Acad Sci U S A 109:18761-18766.
41. Dick, R. A., M. Barros, D. Jin, M. Losche, and V. M. Vogt. 2016. Membrane Binding of the Rous Sarcoma Virus Gag Protein Is Cooperative and Dependent on the Spacer Peptide Assembly Domain. J Virol 90:2473-2485.

42. Gaffney, B. J. 1976. The chemistry of spin labels. Spin Labeling: Theory and Applications L. J. Berliner, ed.:182-238.
43. Khelashvili, G., H. Weinstein, and D. Harries. 2008. Protein diffusion on charged membranes: A dynamic mean-field model describes time evolution and lipid reorganization. Biophysical Journal 94:2580-2597.
44. Khelashvili, G., and D. Harries. 2010. Modeling Signaling Processes across Cellular Membranes Using a Mesoscopic Approach. Ann Rep Comp Chem 6:237-261.
45. Khelashvili, G., M. Doktorova, M. A. Sahai, N. Johner, L. Shi, and H. Weinstein. 2015. Computational modeling of the N-terminus of the human dopamine transporter and its interaction with PIP2 -containing membranes. Proteins 83:952-969.
46. Khelashvili, G., A. Galli, and H. Weinstein. 2012. Phosphatidylinositol 4,5-biphosphate (PIP(2)) lipids regulate the phosphorylation of syntaxin N-terminus by modulating both its position and local structure. Biochemistry 51:7685-7698.
47. Khelashvili, G., D. Harries, and H. Weinstein. 2009. Modeling membrane deformations and lipid demixing upon protein-membrane interaction: the BAR dimer adsorption. Biophys J 97:1626-1635.
48. Andelman, D. 1995. Electrostatic properties of membranes: The Poisson-Boltzmann theory. . Lipowsky, R., Sackmann, E., editors. Amsterdam: Elsevier Science B.V.
49. Chaikin, P., and T. Lubensky. 2000. Principles of Condensed Matter Physics. Cambrige University Press.
50. Baker, N. A., D. Sept, S. Joseph, M. J. Holst, and J. A. McCammon. 2001. Electrostatics of nanosystems: application to microtubules and the ribosome. Proc Natl Acad Sci U S A 98:10037-10041.
51. Davis, I. W., A. Leaver-Fay, V. B. Chen, J. N. Block, G. J. Kapral, X. Wang, L. W. Murray, W. B. Arendall, 3rd, J. Snoeyink, J. S. Richardson, and D. C. Richardson. 2007. MolProbity: all-atom contacts and structure validation for proteins and nucleic acids. Nucleic Acids Res 35:W375-383.
52. Perkins, S. J. 1986. Protein volumes and hydration effects. The calculations of partial specific volumes, neutron scattering matchpoints and 280-nm absorption coefficients for proteins and glycoproteins from amino acid sequences. Eur J Biochem 157:169-180.
53. Efimova, Y. M., A. A. van Well, U. Hanefeld, B. Wierczinski, and W. G. Bouwman. 2004. On the neutron scattering length density of proteins in H(2)O/D(2)O. Physica B 350:E877-E880.
54. Kucerka, N., M. P. Nieh, and J. Katsaras. 2011. Fluid phase lipid areas and bilayer thicknesses of commonly used phosphatidylcholines as a function of temperature. Biochim Biophys Acta 1808:2761-2771.
55. Pan, J., X. Cheng, L. Monticelli, F. A. Heberle, N. Kucerka, D. P. Tieleman, and J. Katsaras. 2014. The molecular structure of a phosphatidylserine bilayer determined by scattering and molecular dynamics simulations. Soft Matter 10:3716-3725.
56. Lorizate, M., T. Sachsenheimer, B. Glass, A. Habermann, M. J. Gerl, H. G. Krausslich, and B. Brugger. 2013. Comparative lipidomics analysis of HIV-1

particles and their producer cell membrane in different cell lines. Cell Microbiol 15:292-304.
57. van Meer, G., D. R. Voelker, and G. W. Feigenson. 2008. Membrane lipids: where they are and how they behave. Nat Rev Mol Cell Biol 9:112-124.
58. Murate, M., and T. Kobayashi. 2016. Revisiting transbilayer distribution of lipids in the plasma membrane. Chem Phys Lipids 194:58-71.
59. Edholm, O., and J. F. Nagle. 2005. Areas of molecules in membranes consisting of mixtures. Biophys J 89:1827-1832.
60. Kucerka, N., B. van Oosten, J. Pan, F. A. Heberle, T. A. Harroun, and J. Katsaras. 2015. Molecular structures of fluid phosphatidylethanolamine bilayers obtained from simulation-to-experiment comparisons and experimental scattering density profiles. J Phys Chem B 119:1947-1956.
61. Eldho, N. V., S. E. Feller, S. Tristram-Nagle, I. V. Polozov, and K. Gawrisch. 2003. Polyunsaturated docosahexaenoic vs docosapentaenoic acid-differences in lipid matrix properties from the loss of one double bond. J Am Chem Soc 125:6409-6421.
62. Heberle, F. A., R. S. Petruzielo, J. Pan, P. Drazba, N. Kucerka, R. F. Standaert, G. W. Feigenson, and J. Katsaras. 2013. Bilayer thickness mismatch controls domain size in model membranes. J Am Chem Soc 135:6853-6859.